EMU Notes in Mineralogy, Vol. 21 (2024), Chapter 6, 155–188

The role of H_2O in the deformation and microstructural evolution of the upper mantle

KÁROLY HIDAS[1] and JOSÉ ALBERTO PADRÓN-NAVARTA[2,3]

[1]*Instituto Geológico y Minero de España (IGME), CSIC, E-18006 Granada (Granada),*
Spain, e-mail k.hidas@igme.es
[2]*Instituto Andaluz de Ciencias de la Tierra (IACT), CSIC, E-18100 Armilla (Granada),*
Spain, e-mail alberto.padron@csic.es
[3]*Géosciences Montpellier, Université de Montpellier & CNRS, F-34095 Montpellier*
cedex 5, France

In this chapter, we evaluate how the incorporation of H_2O as a thermodynamic component influences phase relations in a peridotite composition. This component – present either in the form of hydrous minerals, aqueous fluids and hydrous melts, or as a structurally-bonded trace element at defect sites of nominally anhydrous minerals (NAMs) – may influence upper-mantle rheology in diverse ways. By presenting various natural cases, we identify key incorporation mechanisms and assess their role in the microstructural evolution of ultramafic rocks at different depths in the Earth's interior. These data suggest that the influence of either aqueous fluids or hydrous melts on rheology outmatches that of NAMs or stable hydrous phases across much of the lithospheric mantle. Consequently, future research is expected to shift towards a better understanding of the transient conditions in the lithosphere that control the availability and transport of aqueous fluids and hydrous melts. These transient conditions are likely to play a more dominant role than the sole ability of hydrous defects in NAMs – a role that is currently less well-constrained experimentally – in controlling the ductile deformation of the upper mantle.

1. Introduction: the addition of H_2O as a component to the upper mantle

Mantle deformation governs the most important large-scale geological processes, such as plate tectonics (Fig. 1), on Earth and in other terrestrial planets because the rheological properties of the mantle have a first-order influence on how this deformation is accommodated at great depth (*e.g.* Karato, 2010). It is widely accepted that the rheology of subsolidus peridotite is essentially controlled by the crystal plasticity of olivine, which is the most abundant and the weakest mineral phase in all prevalent lithologies in the upper mantle (Karato and Wu, 1993; Bürgmann and Dresen, 2008). However, despite decades of intense research, processes allowing for ductile deformation of the upper mantle remain poorly understood, yet the role of volatiles has been of interest since the earliest experimental works. The reason is that even the smallest quantities of fluids potentially weaken the rheology (see Kohlstedt and Hansen, 2015 for an overview), and – given that a completely dry and refractory upper mantle can be considered unlikely – the

DOI: 10.1180/EMU-notes.21.6

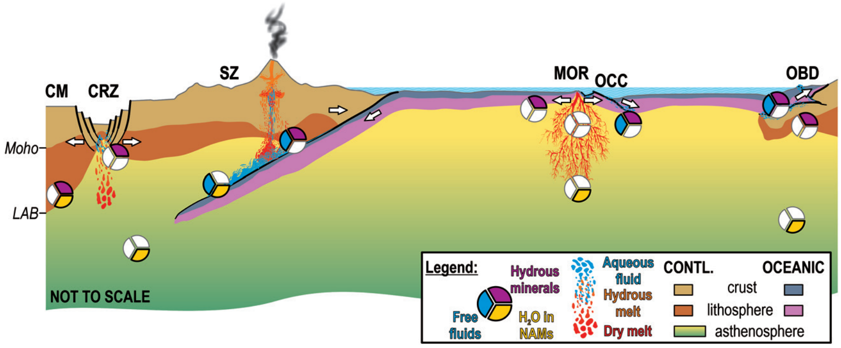

Fig. 1. Schematic cross section of some of the most important plate tectonic settings on Earth. Pie charts indicate the expected dominant forms of the H_2O component to occur in the underlying upper mantle (see text for further details); white slice = irrelevant occurrence. The distribution and provenance of aqueous fluids, hydrous or nominally dry melts along the cross section is theoretical in a given setting. In the present chapter, the actual contribution of various hydrous species to mantle rheology is discussed based on a representative geological record. The figure is not to scale and it may not illustrate the exact tectonic setting of the natural examples cited in the text. Labels of geodynamic environments – CM: cratonic mantle (deep hydrous minerals are mostly controlled by the availability of potassium); CRZ: mantle in continental rift zones; MOR: mantle beneath mid-ocean ridges; OBD: mantle rocks in obduction settings; OCC: mantle in oceanic core-complexes (‘megamullions’); SZ: mantle wedge of subduction zones (hydrous minerals at greater depths than indicated are subject to the availability of potassium). Natural records of the continental mantle are typically exposed in CM, CRZ, OBD and SZ settings, while mantle rocks of the oceanic lithosphere would occur in MOR, OBD, OCC and SZ settings as members of either subduction-unrelated or subduction-accretion (*i.e.* down-going plate) and suprasubduction (*i.e.* upper plate) ophiolites. Other abbreviations – CONTL.: continental; LAB: lithosphere–asthenosphere boundary; Moho: Mohorovičić discontinuity (crust-mantle boundary); NAMs: nominally anhydrous minerals. White arrows show the direction of the main tectonic movements; black lines are undifferentiated brittle, brittle-ductile or ductile tectonic interfaces.

response of the shallow mantle to deformation is probably influenced by the distribution of aqueous fluids and hydrous melts[1] in a fundamental way.

The dominant volatiles of the Earth’s upper mantle are species in the C-O-H system, mostly in the form of H_2O and CO_2 molecular species. However, minor CO, CH_4, H_2, N_2, H_2S and SO_2, electrolytic species, as well as halogens and noble gasses can be present locally (Wyllie and Ryabchikov, 2000; Zhang *et al.,* 2009; Klemme and Stalder, 2018; Mysen, 2022). In this chapter, the attention will be focused on phases containing the H_2O component, and we therefore refer to H_2O as a thermodynamic component of the system. The main pathways to supply this hydrous component to the upper mantle are:

---

[1] Aqueous fluids are H_2O-rich solutions, and hydrous melts are melts with dissolved H_2O content. The two behave as immiscible “phases” at low to intermediate pressure. In general, with increasing pressure, aqueous fluids tend to dissolve more silicate components and hydrous melts more H_2O, until reaching the second critical endpoint of the system, beyond which no difference exists between hydrous melts and aqueous fluids (*e.g.* Bureau and Keppler, 1999; Manning, 2004a,b; Hermann *et al.,* 2006). For the particular case of the H_2O-mantle system, the pressure and temperature conditions of the second critical endpoint are poorly constrained and range from ~3 to 13 GPa and from 950 to 1150°C (*e.g.* Melekhova *et al.,* 2007; Mibe *et al.,* 2007; Wang *et al.,* 2020 and references therein).

(1) the direct crystallization of hydrous minerals, (2) the incorporation of hydrogen (more specifically compensated protons) through point defects in the crystal structure of nominally anhydrous minerals (NAMs), and (3) the percolation of aqueous fluids or hydrous melts at mantle depths (Fig. 1). Ultimately, the source and distribution of this H_2O component is largely controlled by subduction zones and dehydration processes in the slab.

The exact role of each of the above processes in controlling the rheology of the upper mantle is, however, controversial. Some of these controversies stem from an unclear identification of the H_2O-bearing phases that might actually control the deformation processes, both in nature and in experiments. From an experimental perspective (*e.g.* Hirth and Kohlstedt, 2003) the effect of H_2O on the strain rate ($\dot{\epsilon}$) for a given stress (σ) in a 'wet' rheology is usually accounted for by the water fugacity f_{H_2O} term. For example (disregarding the effect of partial melts or oxygen fugacity, Kohlstedt and Hansen, 2015),

$$\dot{\epsilon}(T, P) = \mathrm{A_w}\sigma^n d^{-p} f^r_{\mathrm{H_2O}}(T, P)\exp\left(-\frac{E^*_w + PV^*_w}{\mathrm{R}T}\right) \tag{1}$$

where A_w is a constant for the 'wet' rheology, n is the exponent of the stress term, d is the grain size with a p exponent, r is the exponent of the H_2O fugacity term, E^*_w and V^*_w are the activation energy and volume terms under 'wet' conditions, respectively (Mei and Kohlstedt 2000a,b) and R is the universal gas constant. While the f_{H_2O} term offers a quantitative means to constrain the influence of H_2O on deformation (*cf.* Eq. 1) – which is highly appreciated, *e.g.* in geodynamic modelling – it may obscure the underlying physical processes that govern weakening. Moreover, the widespread use of ambiguous terms in the literature – such as water-saturated and water-undersaturated conditions, water activity, 'hydrous' deformation, 'water' or hydrolytic weakening, and notably, the direct substitution of the f_{H_2O} term in Eq. 1 by 'water' content in olivine (C_{OH}, as discussed by Karato and Jung 2003) – contributes to the overall lack of clarity regarding the actual weakening mechanism. This results in a limited significance of its use as a quantitative parameter in flow laws. The recognition that the term f_{H_2O} in a fluid-rock system – arbitrarily defined from an intensive variable, the H_2O chemical potential (μH_2O) – does not depend solely on pressure and temperature (as implicitly stated in Eq. 1), but fundamentally relies on the relative proportion of H_2O content in the system under consideration, serves as a cautionary note when applying Eq. 1. In an attempt to clarify these ambiguities, a set of definitions illustrated in simple binary and ternary systems including H_2O as a component is presented below.

1.1. H_2O as a thermodynamic component

The thermodynamic description of a system where chemical reactions – in the present case, hydration, dehydration and hydrous melting – are feasible, requires the definition of a 'compositional space'. This compositional space constitutes the minimum set of components necessary to adequately describe (or, more accurately, 'model') the chemical variability of the system and its constituent phases (Spear, 1995). The definition of the system components is arbitrary, with the only constraint that they need to be linearly independent (*i.e.* linear combinations among components are not allowed). For example, in pure molecular fluids (*i.e.* those consisting of species without charge), the choice of including the two components H_2 and O_2 or, alternatively, the single component H_2O as part of the compositional space depends on whether one intends to model or not, respectively, redox reactions among fluid/melt species and solids. Assuming electrical neutrality and ignoring redox reactions, H_2O serves as a convenient thermodynamic component to describe phase relations among H_2O-bearing melts, aqueous fluids, hydrous minerals, and even NAMs as discussed below. The common use of the term 'water' to refer to the H_2O component, although colloquial, is not appropriate because (1) 'thermodynamic components' are just entities of the compositional space and lack of any physical meaning, and (2) 'water' is a phase with a well-defined and limited pressure and temperature stability, which falls well below the conditions commonly encountered in the upper mantle. Therefore, in this book chapter, we prefer to apply the H_2O tag, which should be understood as the colloquial 'water' term, widely – and perhaps unfortunately – used in the mantle literature.

There is no consensus in the literature regarding the terminology for expressing the amount of the H_2O component in hydrated minerals like NAMs, where protons typically balance vacancies and associate with oxygen to form hydroxyl groups (OH^-). However, adopting a consistent approach – as employed for nominally hydrous phases such as amphibole and serpentine that also possess structural hydroxyl groups – justifies the use of H_2O as a thermodynamic component for NAMs too. This becomes more evident when considering the representation of hypothetical hydrous endmembers in NAMs, such as $Mg_2H_4\square O_4$ (defined in terms of MgO and H_2O components) in the case of forsterite, where the empty square indicates a vacancy in the tetrahedral site that satisfied charge balance (Jollands *et al.,* 2023).

1.2. The H_2O chemical potential

The computation of equilibrium phase diagrams enables the definition of the chemical potential of all components in the system (*e.g.* Powell *et al.,* 2019), including H_2O. From a computational perspective, a phase diagram can be constructed by changing either the 'quantity' of the H_2O component (as an extensive variable[2]), or the H_2O chemical potential (as an intensive variable[3]). When the amount of the H_2O component is selected as an independent variable, the H_2O chemical potential becomes a dependent variable[4] with a numerical value that is a function of pressure, temperature and, importantly, phase assemblage. Therefore, from that very moment, the H_2O chemical potential

---

[2] an extensive variable (*e.g.* mass, entropy, or volume) scales with the size or extent of the system. For most purposes we are interested in the state of the system and the relative proportion of its phases; thus the mass of the components is normalized to the total mass of the system. For example, the specific variable $X(H_2O)$ – that is the molar fraction of H_2O in the system (see Fig. 2) – is sufficient to compute the stable phases and their relative proportions.

[3] an intensive variable (*e.g.* temperature, pressure, density, concentration, or chemical potential) is not influenced by the size or extent of the system.

[4] a dependent variable changes in the function of independent variables of the system.

is intrinsically linked to the bulk chemical composition and, in our particular case, the amount of H_2O present in the system in question. From an experimental perspective, the H_2O chemical potential is also a dependent variable unless the experimenter deliberately imposes H_2O fluid saturation, or induces saturation with a fluid containing another non-reacting component in the solution (*e.g.* Ar; for a comprehensive discussion see the seminal work of Greenwood, 1961). In this latter case, the non-reacting component results in a fixed chemical potential of the H_2O component at the run conditions, which would be lower than the chemical potential of a pure fluid containing only H_2O at the same conditions (*i.e.* imposing an H_2O activity lower than one). Thus, the H_2O chemical potential is equal to that of pure H_2O – or, in the buffered experiments, the chosen fixed chemical potential of the H_2O component – exclusively in this situation. It is also experimentally feasible to establish a numerical value for the H_2O chemical potential by introducing hydrous solid phases as H_2O-buffers, as discussed by Otsuka and Karato (2011). However, this approach is constrained to discontinuous values, dictated by the buffering effect observed in specific H_2O-undersaturated mineral assemblages. Notably, Otsuka and Karato (2011) investigated such buffering effects in mineral combinations like clinohumite–periclase–forsterite and brucite–periclase (see the following section).

1.2.1. The H_2O component in a simple MgO-H_2O system

Figure 2 shows a simple MgO-H_2O system computed at constant pressure and temperature conditions to illustrate: (1) the geometric definition of the μH_2O (*i.e.* the H_2O chemical potential); (2) derive corresponding values for a_{H_2O} (*i.e.* the H_2O activity) and f_{H_2O} (*i.e.* the H_2O fugacity); and (3) show their dependence on $X(H_2O)$ (*i.e.* the relative amount of H_2O). In this system, there are no solid solutions, and the determination of stable phases involves the computation of their Gibbs energies per mol of components in the system (number of mols of H_2O and MgO in each phase) under the specified pressure and temperature (P-T) conditions. Subsequently, the identification of stable phases is achieved by locating the minimum surface defined by two phases: periclase-brucite and brucite-H_2O in Fig. 2a, and periclase-H_2O in Fig. 2b. Notably, in the latter case, the appearance of brucite above the line connecting periclase-H_2O indicates that the univariant reaction brucite = periclase + H_2O has been crossed at the corresponding P-T conditions, and brucite is no longer stable. Once the stable phases are found, it is possible to compute the two chemical potentials by extending the line that joins the two phases until its intersection with the vertical axis of the two system components (*i.e.* MgO-H_2O) at $X(H_2O) = 0$ for the MgO component, and at $X(H_2O) = 1$ for the H_2O component. By definition, both chemical potentials (μMgO and μH_2O) are equal for each of the individual two-phase assemblages that are stable (*e.g.* per-br and br-H_2O in Fig. 2a define a total of two different pairs of μH_2O and μMgO). Each two-phase assemblage defines, therefore, a unique μH_2O. In the illustrated example in Fig. 2a, considering the periclase-brucite assemblage, the line joining these two stable phases (solid black line) is extended until it intersects with the vertical axis at $X(H_2O) = 1$ (dashed violet line). This intersection point occurs at –268,844 J/mol (depicted as a violet dot in Fig. 2a), and it defines the H_2O chemical potential of periclase-brucite ($\mu_{H_2O}^{per-br}$) at 2 GPa and 500°C. Note that $\mu_{H_2O}^{per-br}$ is lower than the chemical

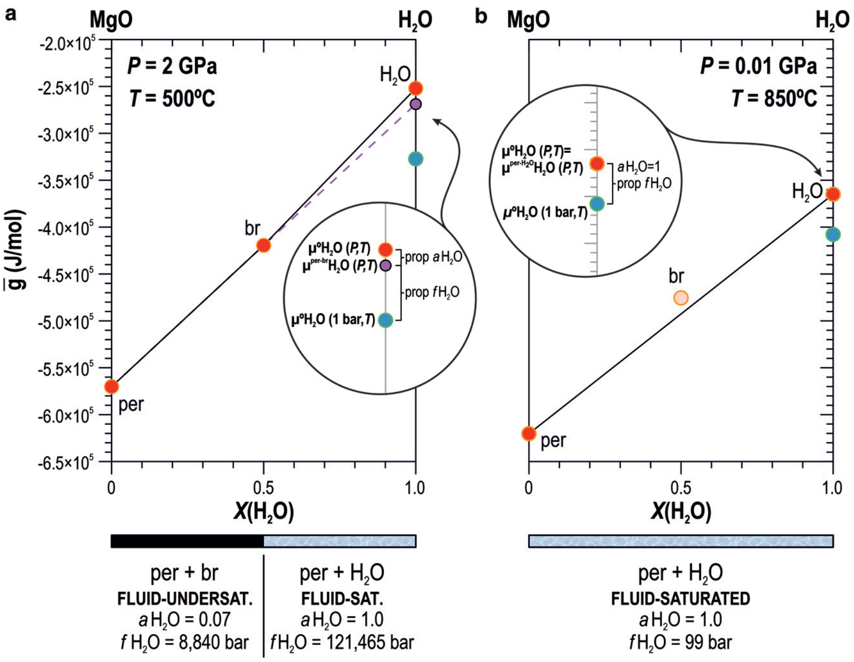

Fig. 2. Definition of the thermodynamic H_2O chemical potential (μH_2O) for two distinct two-phase assemblages within the MgO-H_2O system: periclase-brucite, $\mu_{H_2O}^{per-br}$ at 2 GPa and 500°C (773 K) in (***a***) and $\mu_{H_2O}^{per-H_2O}$ at 0.01 GPa and 850°C (1123 K) in (**b**). Also depicted are their two arbitrarily derived quantities: H_2O activity (a_{H_2O}) proportional to the difference between the μH_2O of the phase-assemblage and the chemical potential of the pure H_2O at the same P,T conditions, $\mu_{H_2O}^{\circ}$ (P,T) (see Eq. 2); and H_2O fugacity (f_{H_2O}), relative to 1 bar and the same temperature, $\mu_{H_2O}^{\circ}(1\text{ bar}, T)$ (see Eq. 3). Note that the μH_2O (and all derived quantities) is composition-dependent – expressed as $X(H_2O)$ or $H_2O/(H_2O + MgO)$ in molar fractions – in (**a**), but not in (***b***), where fluid saturation occurs for all compositions, and periclase and H_2O are more stable than brucite (partially transparent circle). The vertical axis ($\bar{g}$ in J/mol) represents the Gibbs energy of the phase per mol of components in the system (*i.e.* the sum of mole of H_2O and MgO in the stoichiometric formula of the phase). The figure was computed using *Perple_X* (Connolly, 2009) and the Holland and Powell (2011) thermodynamic dataset. The equation of state for H_2O is from Pitzer and Steiner (1994). prop: proportional to.

potential of pure H_2O ($\mu_{H_2O}^{o}$) at the same conditions, which is situated at –252,003 J/mol and is depicted as a red dot at $X(H_2O) = 1$ in Fig. 2a. Consequently, all compositions ranging from $X(H_2O) = 0$ to 0.5 (corresponding to the compositional periclase-brucite joint) are fluid undersaturated and exhibit identical μH_2O. The difference in energy between the pure H_2O at the given P-T conditions – denoted as $\mu_{H_2O}^{o}$(P,T) and $\mu_{H_2O}^{per-br}$(P,T) – defines the H_2O activity (a_{H_2O}), as given by Eq. 2.

$$a_{H_2O} = \exp\left(\frac{\mu_{H_2O}^{per-br}(P,T) - \mu_{H_2O}^{\circ}(P,T)}{\mathrm{R}T}\right) \tag{2}$$

In the specific case depicted in Fig. 2a,

$$a_{\mathrm{H_2O}} = \exp\left(\frac{-268{,}844\,\mathrm{J\cdot mol^{-1}} - (-252{,}003\,\mathrm{J\cdot mol^{-1}})}{8.3145\,\mathrm{J\cdot mol^{-1}\cdot K^{-1}}\cdot 773\,\mathrm{K}}\right) = 0.073$$

Figure 2b shows the same MgO-H_2O system at lower P (0.01 GPa) and higher T (850°C) conditions, where H_2O saturation is achieved. As evident in the figure, at H_2O saturation, both H_2O chemical potentials – *i.e.* $\mu^{\circ}_{\mathrm{H_2O}}(P, T)$ and $\mu_{\mathrm{H_2O}}^{\mathrm{per-H_2O}}(P,T)$, depicted as a red dot at $X(\mathrm{H_2O}) = 1$ – are identical, hence the H_2O activity equals to one ($a_{\mathrm{H_2O}} = 1$), according to Eq. 2.

In contrast to the reference used in the definition of H_2O activity ($a_{\mathrm{H_2O}}$) at the P-T conditions of interest, the H_2O fugacity ($f_{\mathrm{H_2O}}$) is defined relative to the H_2O chemical potential at the temperature of interest, yet at a reference pressure of 1 bar, denoted as $\mu^{\circ}_{\mathrm{H_2O}}(1\ \mathrm{bar}, T)$. In the studied MgO-$H_2O$ system at 2 GPa and 500°C (Fig. 2a), the $f_{\mathrm{H_2O}}$ can be calculated as shown in Eq. 3.

$$f_{\mathrm{H_2O}} = f^{\circ}_{\mathrm{H_2O}} \exp\left(\frac{\mu_{\mathrm{H_2O}}^{per-br}(P,T) - \mu^{\circ}_{\mathrm{H_2O}}(1\ \mathrm{bar}, T)}{\mathrm{R}T}\right) \qquad (3)$$

where $f^{\circ}_{\mathrm{H_2O}}$ is the standard state fugacity at the reference pressure and equals 1 bar. Thus, for the H_2O-undersaturated conditions shown in Fig. 2a (at $X(\mathrm{H_2O}) = 0.0$–0.5), we have:

$$f_{\mathrm{H_2O}} = 1\,\mathrm{bar}\cdot\exp\left(\frac{-268{,}844\,\mathrm{J\cdot mol^{-1}} - (-327{,}247\,\mathrm{J\cdot mol^{-1}})}{8.3145\,\mathrm{J\cdot mol^{-1}\cdot K^{-1}}\cdot 773\,\mathrm{K}}\right)$$
$$= 8840\,\mathrm{bar}\,(0.88\,\mathrm{GPa})$$

At the H_2O saturation condition shown in Fig. 2b, the $f_{\mathrm{H_2O}}$ can be computed directly by determining the difference between $\mu^{\circ}_{\mathrm{H_2O}}(P,T)$ and $\mu^{\circ}_{\mathrm{H_2O}}(1\ \mathrm{bar}, T)$. Importantly, this calculation is solely dependent on the pressure and temperature of the system, and it remains unaffected by $X(\mathrm{H_2O})$ (*i.e.* for $X(\mathrm{H_2O}) > 0.5$ in Fig. 2a, and for all $X(\mathrm{H_2O})$ values in Fig. 2b). It is crucial to realize that without knowledge of the stability conditions of brucite – specifically without Gibbs energy minimization of the full system – establishing *a priori* whether fluid saturation conditions are met is not possible. Consequently, $\mu_{\mathrm{H_2O}}, f_{\mathrm{H_2O}}$ and $a_{\mathrm{H_2O}}$ cannot be computed solely based on a chosen P-T condition if this information is lacking. In experimental works, employing Eq. 1 directly, using $f_{\mathrm{H_2O}}$ from the equation of state (EoS) for pure H_2O at the running pressure and temperature conditions assumes that hydrous phases, hydrous melt or H_2O in NAMs are equilibrated with excess H_2O, and such an approach implicitly considers H_2O saturation.

1.2.2. The H_2O component in solid solutions in the MgO-SiO_2-H_2O system

The aforementioned approach gains greater relevance for a mantle composition when extended to the MgO-SiO_2-H_2O system. This extension enables the exploration of the implications of incorporating solid solutions, such as hydrous melts and NAMs with variable compositions. In this context and for illustrative purposes, the continuous Gibbs energy is piecewise linearized using pseudocomponents (*i.e.* discrete compositions along the solid solution that are considered as discrete phases), as outlined by Connolly and Kerrick (1987). Solid solution models for NAMs are still under development (Padrón-Navarta, 2019).

For didactic purposes, a simplified example for forsterite is presented in a sandbox environment, considering only protons associated with oxygen in silicon vacancies ($Mg_2H_4\square O_4$, where the empty square indicates a vacancy; see Jollands *et al.*, 2023 for further details), and referred here to as hydrous forsterite (hfo), a hypothetical endmember. To facilitate a more straightforward analysis in 2D plots, the system can be projected conveniently from enstatite[5], as illustrated in Fig. 3 (purple arrows in the ternary diagrams showing the direction of projection from enstatite). Despite its simplicity, this system allows the definition of three crucial types of phase relations. At extremely low H_2O concentrations, the only stable phase is hydrous forsterite (and enstatite) at all temperatures, as depicted by the blue region in the compatibility diagrams in Fig. 3. It is noteworthy that in this single-phase field (hfo), there is a continuous increase in H_2O content of hydrous forsterite with increasing $X(H_2O)$ (see inset in Fig. 3a for an enlarged view; the same process applies to Fig. 3b–c), with tangents to its energy ω-surface approximated by two pseudocomponents. In the example, the tangent line shown in Fig. 3a is defined by hfo_1 and hfo_2 (pale blue circles labeled accordingly in the inset of the figure). In any other two-phase assemblage involving hydrous forsterite – *i.e.* hfo + atg in Fig. 3a, hfo + H_2O in Fig. 3b and hfo + melt in Fig. 3c –, the H_2O content in forsterite does not increase with increasing $X(H_2O)$, and the composition of hfo is fixed. At low temperatures, the hydrous phase antigorite is stable. Antigorite has a lower Gibbs energy than pure H_2O and one of the pseudocomponents from hydrous forsterite (*i.e.* hfo_3 in Fig. 3a). Thus, it plots in a lower position in the diagram than a metastable line joining them (Fig. 3a). As temperatures increase, antigorite is no longer stable, resulting in a simplified compatibility diagram (Fig. 3b) with only two fields (+enstatite): hydrous forsterite, and hydrous forsterite+H_2O, depicting H_2O-undersaturated and H_2O-saturated conditions, respectively. These regions are divided by one pseudocomponent (equivalent to hfo_3[6]). This scenario is important, as only a relatively small amount of H_2O – greater than the solubility of H_2O in the NAMs – would be enough to reach H_2O saturation, which has significant implications for the interpretation of hydrous deformation experiments.

At the highest temperatures, the hydrous melt surface intersects the H_2O-hfo joint, resulting in four regions. As a consequence, hydrous forsterite is no longer stable with pure H_2O (Fig. 3c). In the hfo + melt region, the H_2O content in olivine is buffered by the hydrous melt and does not increase with the H_2O content of the system, because

---

[5] although this has the drawback that certain fields at lower temperatures are metastable relative to talc, and compositions of melts with silica contents exceeding those in enstatite cannot be considered. The avid reader would find that the latter issue renders the melt + H_2O (+en) field represented in Fig. 3c metastable in the full MgO-SiO_2-H_2O system.

[6] it is customary to give a special term to the composition of this pseudocomponent as it represents the 'solubility' or maximum H_2O content in the NAMs at H_2O-saturation at these pressure and temperature conditions.

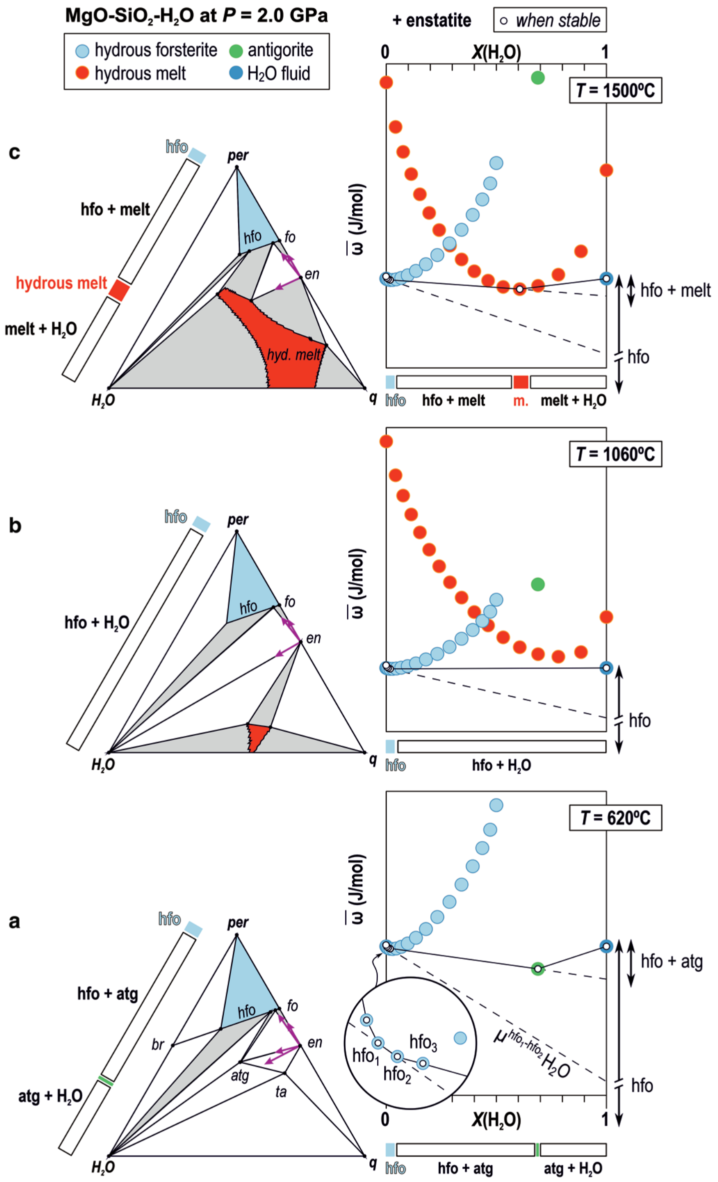

Fig. 3. General phase relations for an enstatite-saturated MgO(forsterite)-H_2O system at constant 2 GPa pressure and various temperatures, involving a H_2O phase, a hydrous phase (antigorite), a hydrous melt, and a hydrous forsterite (hfo) solid solution (Mg_2SiO_4-$Mg_2H_4\square O_4$) representing a NAM, created here for didactic purposes only. (***a***) Low temperature (620°C) where antigorite is stable, (***b***) medium temperature (1060°C) above the dehydration of antigorite, and (***c***) high temperature (1500°C) above the wet hydrous melting. Gibbs energies (designated as ω) are plotted after projection from enstatite as a function of $X(H_2O)$, now defined as H_2O /(MgO' + H_2O) in mol units, where MgO' is MgO after projection from enstatite

the system is divariant. This situation may also be relevant for deformation experiments involving a small degree of hydrous partial melting. In such cases, the f_{H_2O} cannot be directly computed from the *P-T* conditions, but the inclusion of a solubility model for H_2O in the melt – dictating the H_2O chemical potential – is needed (*cf.* Hirth and Kohlstedt, 1996; Asimow *et al.*, 2004).

Figure 4 illustrates a *T-X*(H_2O) diagram for the entire MgO-SiO_2-H_2O system, maintaining a constant MgO/SiO_2 ratio at a fixed pressure of 2 GPa, within a small range of bulk H_2O contents (0.0–0.4 mol.%; equivalent to 0–1470 ppm wt. H_2O), representing conditions typical of the upper mantle. These simple diagrams bring a novel perspective by examining the impact of H_2O in NAMs on the chemical potential of H_2O (panel 2) and other derived variables under H_2O-undersaturated conditions in a thermodynamically consistent manner, as opposed to iterative calculations (*cf.* Hirth and Kohlstedt, 1996; Asimow *et al.,* 2004). In the H_2O-undersaturated region, where hydrous phases or hydrous melts are not stable (shown as a semi-transparent field in Fig. 4), the chemical potential depends on the incorporation of H_2O in into the hydrous forsterite, which thus controls all dependent quantities (*i.e.* H_2O activity and H_2O fugacity). Suffice to say that experiments aimed at investigating the rheological effect of H_2O incorporated in the structure of olivine should be conducted specifically within this *T*(*P*) and *X* (H_2O) window. Unfortunately, this window is poorly constrained in natural systems, primarily due to the dependence of H_2O incorporation into NAMs on various factors, such as trace element concentration and oxygen fugacity (*e.g.* Tommasi *et al.,* 2017). It has been suggested that the correlation of the strain rate with H_2O fugacity can be used to support the equivalent effect of H_2O concentration in NAMs on strain rate (*e.g.* Hirth and Kohlstedt, 2003; Karato and Jung, 2003; Kohlstedt and Hansen, 2015). The f_{H_2O} is very sensitive to changes in *P* and *T* under H_2O-saturated conditions; therefore, the fact that this dependency is identified when considering data at different *P-T* conditions does not, by itself, demonstrate that the dependency of f_{H_2O} (or H_2O content in olivine) can be quantified (but see Faul *et al.,* 2016).

Fig. 3. *Continued.* ($Mg_2Si_2O_6$). The projection is shown as purple arrows in the ternary diagrams. In this projection, antigorite ($Mg_{48}Si_{34}O_{85}(OH)_{62}$) has the following composition: en = 17, MgO' = 14, and H_2O = 31 in the new component system, and thus plots at $X(H_2O) = 31/45$ (green circles). Stable phases are defined by the minimum ω surface (indicated by white circles), i.e. the Legendre transform of the molar Gibbs energy. For example, g^{atg} is transformed to ω^{atg} through the expression $\omega^{atg} = (g^{atg} - X_{en}\mu^{en})/(1 - X_{en})$, where $X_{en} = \mathrm{en}/(\mathrm{en} + \mathrm{MgO'} + H_2O)$ in mol ratio and g^{atg} is the Gibbs energy of atg in the new component system (en-MgO'-H_2O, 17-14-31). Dashed lines represent extrapolation to $X(H_2O) = 1$ of the indicated two-phase assemblages (or two-pseudocomponents in the case of the single-phase hydrous forsterite, hfo). The vertical arrows show their differences relative to the chemical potential of pure H_2O ($\mu^{\circ}_{H_2O}$), proportional to the activity of H_2O through Eq. 2. Although the diagram is quantitative, the values of ω have been corrected by a factor proportional to $X(H_2O)$ and the difference between the energies of forsterite and H_2O to better illustrate stable phases. At the bottom of each diagram, a schematic compatibility diagram is shown, illustrating the stable phases. In the ternary diagrams, abbreviations are: atg – antigorite, br – brucite, en – enstatite, fo – forsterite, hfo – hydrous forsterite, per – periclase, q – quartz, ta – talc, solid solutions (melt and hydrous forsterite) are represented as pseudocomponents (red and pale blue, respectively).

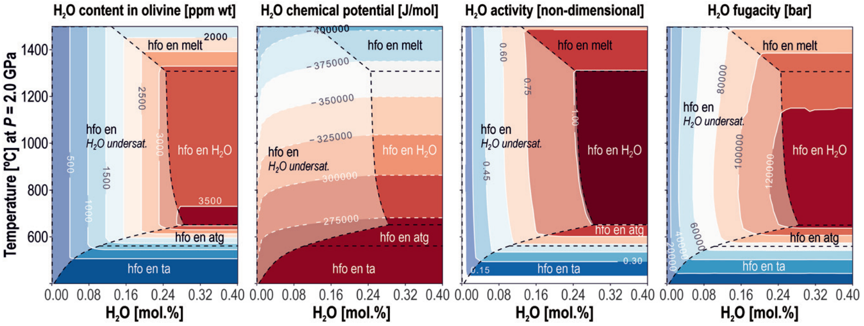

Fig. 4. Pseudosections of temperature *vs.* molar percentage of H_2O at a constant pressure of 2 GPa, maintaining a constant MgO/SiO_2 ratio of 0.55/0.45 mol, and increasing H_2O along the horizontal axis at low bulk H_2O contents (up to 0.40 mol%, equivalent to 1470 ppm wt. H_2O). Superimposed on all diagrams are the boundaries of the equilibrium field assemblages, in which the stable phases are indicated as follows: atg – antigorite; en – enstatite; hfo – hydrous forsterite; ta – talc ($\pm H_2O$ or melt). All fields are divariant (three-phases in a three-component system), except for the two-phase assemblage consisting of hydrous forsterite and enstatite, which is highlighted with semi-transparency (see also Fig. 3). This latter field corresponds to H_2O undersaturated conditions without the presence of hydrous phases or melt. It is important to note that, by definition, only in this two-phase field does the H_2O chemical potential (and derived H_2O activity and H_2O fugacity values) change with bulk H_2O content at constant T (and P). Thus, this is the only relevant field for deformation experiments addressing the rheological effect of the structurally bonded H_2O component in NAMs. The molar percentage of H_2O is defined here as $H_2O/(MgO+SiO_2+H_2O)$ in mol ratio, and expressed in percent.

1.2.3. The H_2O component in the upper mantle

In the following example, we disregard the effect of solid solution for H_2O in NAMs (as these models are not yet fully available; Padrón-Navarta, 2019), and we focus on the Na_2O-CaO-FeO-MgO-Al_2O_3-SiO_2-H_2O-Cr_2O_3 (NCFMASHCr) system to explore processes that take place in a more realistic mantle composition. Among these components, Na_2O is relevant for the stability of pargasitic amphiboles that – together with NCFMASH melts – exert a primary influence on the H_2O chemical potential. Note that the K_2O component – although not considered in the system discussed in this section – is also important in other settings (see Fig. 1) for the stability of phlogopite and K-richerite amphibole, which are stable at depths >180 km (*e.g.* Konzett and Ulmer, 1999). Figure 5 illustrates that regions saturated in a free H_2O fluid phase (fields with water pattern, where the H_2O activity is = 1 as shown in Fig. 5b,e) become wider at lower pressures. Only in these regions do the H_2O fugacity, the modal content of hydrous phases, and the melt fraction remain independent of the amount of H_2O in the system, as evidenced by the solid horizontal lines in Fig. 5. For the low bulk H_2O contents (0.0–1.0 wt.% H_2O) considered in Fig. 5, which are feasible in various settings in the shallow upper mantle (Fig. 1), most phase assemblages are H_2O-undersaturated with either hydrous melts at high temperature or hydrous phases – such as amphibole or chlorite – at low temperatures. In complex multicomponent systems, these H_2O-undersaturated fields containing hydrous phases or hydrous melts also constrain the values of the H_2O activity and H_2O fugacity, as is done in simpler systems (Fig. 3a, c).

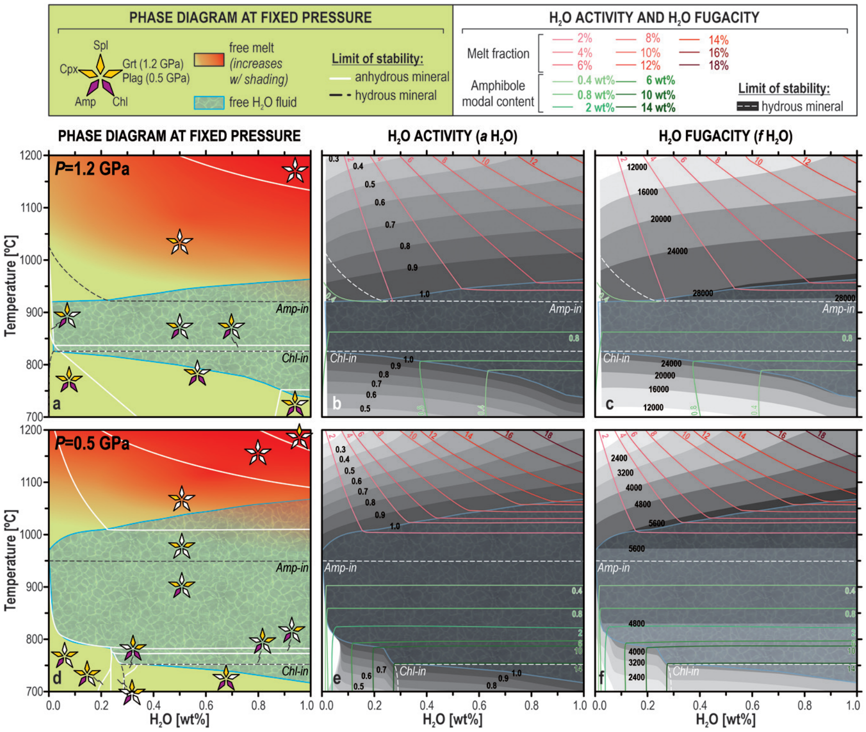

Fig. 5. Calculated pseudosections (colour-shaded diagrams in ***a,d***), as well as H_2O activity (grey-shaded diagrams in ***b,e***) and H_2O fugacity (grey-shaded diagrams in ***c,f***) in the Na_2O-CaO-FeO-MgO-Al_2O_3-SiO_2-Cr_2O_3 system for a harzburgite whole-rock composition (sample RK025 – CaO: 1.74 wt.%; MgO: 41.9 wt.%; Al_2O_3: 1.67 wt.%; SiO_2: 43.8 wt.%; FeO: 7.58 wt.%; Na_2O: 0.02 wt.%; Cr_2O_3: 0.37 wt.%; data from Hidas *et al.,* 2016 from the Ronda massif, Spain) at equilibrium pressures of 1.2 GPa (**a–c**) and 0.5 GPa (***d–f***) as a function of temperature (°C) and H_2O content of the system (wt.%). The computation was carried out in *Perple_X* (Connolly, 2009) using the solid solution models of Holland *et al.* (2018). In (***a,d***), the stable mineral assemblage is indicated by diamond symbols (yellow: nominally anhydrous minerals, purple: hydrous minerals); olivine and orthopyroxene are stable throughout the entire modelled space. Note that at 1.2 GPa, a minor (<30°C) compositional gap between tremolitic and pargasitic amphiboles is predicted by the modelling at low temperature (<770°C) and high bulk H_2O contents (>0.7 wt.%), which is omitted from the figure for simplicity. Increasing melt fraction as a function of temperature and H_2O content is visualized qualitatively in parts **a** and **d** as shading of the melt-bearing field, but quantitative results of the calculation are shown in **b–c** and **e–f**. Black numbers in **b**,**e** and **c**,**f** indicate H_2O activity (dimensionless ranging from 0.0 in white shaded fields to 1.0 in dark grey shaded field) and H_2O fugacity (in bars) values, respectively. H_2O-saturation conditions are met at H_2O activity of 1.0, thus the fields with a free H_2O fluid in **a** and **d** are the same as those with a H_2O activity of 1.0 in **b** and **e**. Note that due to their formal definition, H_2O activity (***b***,***e***) and H_2O fugacity (***c***,***f***) are not equivalent terms and hence their use is not interchangeable. For more details, see section 1.2.1. As a comparison, the limits of stability of hydrous minerals in **a** and **d** (as black dashed lines) are also represented in **b**,**c** at 1.2 GPa and in **e**,**f** at 0.5 GPa (as white dashed lines). In **b**, **c**, **e** and **f**, pink to red coloured solid lines (in the upper half of the figure) and green-shaded solid lines (in the lower half of the figure) represent the volume fraction of melt (vol.%) and the modal content of amphibole (wt.%), respectively. Observe that at relatively low temperatures (~800–900°C), both at pressures of 0.5 GPa and 1.2 GPa, the increase of H_2O component in the bulk-rock composition does not influence the amphibole content and the system remains fluid-saturated, recording relatively small modal amounts of amphibole (<2.0 wt.%).

However, due to the existence of many possible continuous multivariant reactions between all phases (*e.g.* tremolite content in amphibole, anorthite content in plagioclase, chromium in spinel, *etc.*), the values of H_2O activity/fugacity do not vary linearly with the relative amount of H_2O in the system, as opposed to simple systems (*cf.* Fig. 4) because they depend on the amount of hydrous phases or hydrous melts at H_2O-undersaturated conditions (*i.e.* lower half or upper half of the diagrams, respectively). We emphasize that under these H_2O undersaturated conditions, introducing the H_2O fugacity term in rheological constitutive laws (Eq. 1) is unlikely to have any physical meaning without considering all the variables that may influence it, particularly the total H_2O content in the system at the relevant P-T conditions of deformation. The H_2O fugacity can only be computed independently from the chemical complexities of the rock in situations of H_2O saturation, which can only be achieved for realistic low H_2O contents when neither hydrous phases nor hydrous melts are stable, and the H_2O content in the system exceeds that required for H_2O saturation of NAMs (Fig. 4). In any case, it is highly probable that under those circumstances, the rheological behaviour would be more influenced by the presence of a stable interstitial free fluid phase than by the numerical value of the H_2O fugacity, or even the actual H_2O content in the NAMs.

These observations suggest the need for further research focused on a better understanding of the conditions in the upper mantle that control the stability of hydrous minerals, as well as the distribution and composition of aqueous fluids and hydrous melts. Additionally, the solubility of H_2O in NAMs (particularly for pyroxenes with mantle composition) and its dependency on other factors, such as trace elements and eventually fO_2, need to be further constrained. This is important because under natural conditions, their impact on rheology may be major and, perhaps, different than previously thought. Moreover, in future constitutive rheological laws accounting for the effect of hydrous components, it is essential to differentiate clearly between direct measurements of extensive variables (*i.e.* $X(H_2O)$ in the experimental system, as illustrated in Figs 2–5), and dependent intensive parameters (such as H_2O fugacity), the latter being a complex function of the reactive deforming system.

2. Effect of H_2O components on the rheological behaviour and microstructural evolution of the upper mantle: experiments *vs.* nature

In recent decades, many efforts have been made to obtain quantitative experimental data on the rheological behaviour of the upper mantle. Below we review the major achievements that – at least marginally – addressed the potential role of H_2O components presented in Fig. 1, and we summarize what the numerous recent natural case studies demonstrate when these components are inferred to be at play during ductile deformation of the upper mantle.

2.1. Hydrous melt and hydrous minerals

In contrast to anhydrous melts (*e.g.* Hirth and Kohlstedt, 1995a,b; Kohlstedt and Zimmerman, 1996; Bai *et al.,* 1997; Zimmerman *et al.,* 1999; Holtzman *et al.,* 2003a,b;

Zimmerman and Kohlstedt, 2004; Scott and Kohlstedt, 2006; Takei and Holtzman, 2009a,b,c; King *et al.,* 2010; Kohlstedt *et al.,* 2010; Soustelle *et al.,* 2014), there are very few experiments on the mechanical behaviour of hydrous melts during deformation, but available data indicate that the presence of H_2O enhances strain rates by approximately two orders of magnitude compared to equivalent anhydrous systems (Mei *et al.,* 2002). Of particular importance in hydrous melts is that they are common metasomatic agents in the upper mantle, which contribute to the generation of chemical and mineralogical heterogeneities (O'Reilly and Griffin, 2013 and references therein). Amphibole and mica are well-known products of such melt percolation in a wide depth range and in various tectonic settings (*e.g.* Dawson and Smith, 1982; Vannucci *et al.,* 1995; Zanetti *et al.,* 1996; Coltorti *et al.,* 2007; Shaw, 2009; Fumagalli and Klemme, 2015; Mandler and Grove, 2016; Bonadiman *et al.,* 2021; Wang *et al.,* 2021). Moreover, amphibole is the most important H_2O-storing mineral in the upper mantle down to ~3 GPa, ~90–100 km depth in an oceanic environment (Green *et al.,* 2010; Green, 2015), while phlogopite – subject to sufficient potassium – plays a similar role to somewhat deeper levels (Mengel and Green, 1989; Wyllie and Ryabchikov, 2000). The breakdown of amphibole causes a remarkable drop in the solidus temperature of fertile lherzolites and, at the same time, reduces the H_2O-storage capacity of the mantle, which is then controlled only by the NAMs under subsolidus conditions at greater depths (Green *et al.,* 2010; Kovács *et al.,* 2021). Although these results demonstrate that the presence of hydrous minerals controls the H_2O-storage capacity of the mantle at lithospheric mantle depths, to date, natural observations are scarce and no experimental data are available to constrain their implication for the rheology while they are present as stable phases in an otherwise nominally anhydrous, four-phase peridotite. Tommasi *et al.* (2017) provided one of the first microstructural observations from coarse-grained pargasite- and phlogopite-bearing peridotites, which record pervasive ductile deformation in the dislocation creep regime coeval to percolation of hydrous Si-rich melts at mantle depths (980–1080°C and <2 GPa) in the Finero massif (southern Alps, Italy). Their study concurs with the available experimental data (Mei *et al.,* 2002) and shows that the synkinematic presence of interstitial hydrous melts leads to significant rheological weakening of mantle rocks by accommodating large amounts of deformation due to a switch of the deformation mechanisms to stress-controlled dissolution-precipitation creep. However, the lack of correlation of olivine fabric strength and the symmetry of crystallographic-preferred orientation (CPO) – or lattice-preferred orientation (LPO) – of olivine to the occurrence of hydrous minerals (pargasite and/or phlogopite) in the peridotites implies little or no direct effect of these phases on the microstructural evolution of mantle rocks (Fig. 6). Even when hydrous minerals are present in peridotites at modal abundances of up to 25 vol.%, the fabric strength remains relatively weak in the peridotites (Fig. 6). This observation indicates that the mere presence of stable hydrous minerals in peridotites during deformation does not exert a significant influence on the rheological behaviour of the upper mantle (Tommasi *et al.,* 2017). It is conceivable that, as long as hydrous minerals are stable, rather than simply present, it is the saturation of rocks in H_2O and/or hydrous melts that controls the rheology of the mantle. Moreover, it is important to note that hydrous metasomatism does not consistently influence the H_2O content of the

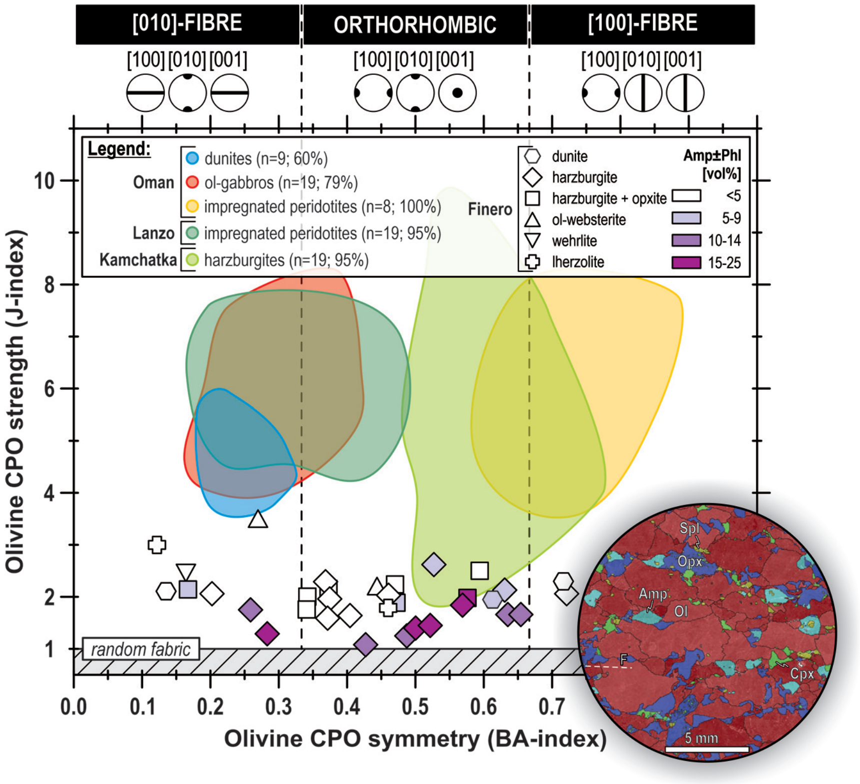

Fig. 6. Olivine crystallographic preferred orientation (CPO) symmetry (BA-index) as a function of the olivine fabric strength (J-index) in pargasite and phlogopite-bearing coarse-grained peridotites from the Finero massif (Tommasi *et al.,* 2017) compared to peridotites deformed in the presence of H_2O-poor basaltic melts (Oman and Lanzo; Higgie and Tommasi, 2012, 2014) or aqueous fluids (Kamchatka; Soustelle *et al.,* 2010), represented as colour-coded fields that cover >60% of the total dataset; *n*: number of samples shown in the field, and the percentage they correspond to compared to the total available dataset. Outliers are not shown for simplicity. Note that the Finero peridotites encompass the entire range of typical olivine CPO symmetries and, despite the microstructure, suggest coeval deformation of anhydrous and hydrous minerals (see inset) and the hydrous minerals display patent CPO (not shown here) consistent with shear deformation in the plane of the foliation (marked by ‘F’ and dashed line in the inset); the overall weak olivine fabric is not correlated to the modal abundance of hydrous minerals. The J-index (Bunge, 1982) is a dimensionless measure of the fabric strength, which takes a value of 1 in a randomly oriented material and it is infinite for a single-crystal orientation; olivine J-indices in mantle peridotites typically range from 2–20 with a peak at ~5 (Tommasi and Vauchez, 2015). The BA-index is a tool to characterize point and girdle-like distribution of olivine [010] and [100] crystallographic axes, which allow for differentiating the three most common olivine CPO symmetries in mantle peridotites (see Mainprice *et al.,* 2014 for more details). Labels – Amp: amphibole, Cpx: clinopyroxene; Ol: olivine; Opx: orthopyroxene; Spl: spinel (after Whitney and Evans, 2010). The original version of this figure was published in “Hydrous melts weaken the mantle, crystallization of pargasite and phlogopite does not: Insights from a petrostructural study of the Finero peridotites, southern Alps”, by Tommasi, A., Langone, A., Padrón-Navarta, J.A., Zanetti, A. & Vauchez, A. in *Earth and Planetary Science Letters,* **477**, 59–72 (2017), Copyright Elsevier.

coexisting NAMs. In cases where hydrous minerals are present, the NAMs – particularly olivine – tend to remain relatively dry or only moderately saturated in H_2O (*e.g.* Denis *et al.,* 2015; Hao *et al.,* 2016; Aradi *et al.,* 2017; Tommasi *et al.,* 2017; Demouchy and Tommasi, 2021).

2.2. Structurally bonded H_2O

The weakening effect of the hydroxyl concentration in NAMs has been known since the earliest experiments on quartz crystals in the 1960s (Griggs and Blacic, 1965; Griggs, 1967; Blacic, 1975), where the decrease in strength of the mineral was observed with increasing hydrogen (proton) concentration and explained by easier movement of dislocations in the wet crystalline lattice. Subsequently, the potential impact of H_2O-linked weakening on mantle rheology has been proposed through experiments on olivine (Avé Lallemant and Carter, 1970) and pyroxene (Avé Lallemant, 1978). Later studies have been focused on the overview of the weakening mechanisms in major constituent phases of mantle peridotites and pyroxenites (*e.g.* Kohlstedt *et al.,* 1995; Mei and Kohlstedt, 2000a,b; Karato and Jung, 2003; Chen *et al.,* 2006; Tielke *et al.,* 2017) and resulted in the widespread acceptance that, in continental environments, the rheology of the lithospheric mantle, in general, and the crust-mantle coupling, in particular, may be controlled by the behaviour of olivine, with variable concentrations of hydrous defects. In the last decade, however, low-*T* (800–1100°C) dry deformation experiments on olivine challenged this paradigm (Demouchy *et al.,* 2013, 2014). These experiments demonstrated that the inferred important weakening effect of hydrous defects is partly due to the large error in the extrapolation of high-*T* ($>$1200°C) deformation experiments to natural conditions prevalent in the shallow lithospheric mantle (~900–1000°C), and so the rheology of dry olivine is indeed significantly weaker at these low-*T* conditions than previously thought. Thus, numerical modelling of lithospheric strength profiles may not need to operate with wet olivine rheology to weaken the lithospheric mantle (Boioli *et al.,* 2015). Currently, there is a general consensus within the scientific community that hydrous defects incorporated into the olivine structure have a discernible weakening effect, at least up to $\sim$18 ppm wt. H_2O concentrations (Girard *et al.,* 2013; Faul *et al.,* 2016). However, it is also acknowledged that the significance of this weakening effect may have been somewhat overestimated in both diffusion (Fei *et al.,* 2013) and dislocation creep regimes (Demouchy *et al.,* 2012; Girard *et al.,* 2013).

As for the microstructural record of deformation at upper mantle conditions, CPO in olivine is often, although not exclusively, induced by deformation flow that activates different dislocation slip systems (*e.g.* Karato, 2008). The resulting CPO patterns are potentially important tracers in seismogenic modelling of the Earth's interior (Tommasi *et al.,* 1999; Mainprice *et al.,* 2000; Karato *et al.,* 2008; Hansen *et al.,* 2021). Natural record shows that the most common CPO symmetries in mantle rocks – developed by simple shear deformation in the dislocation creep regime – are characterized by the [100] olivine crystallographic axes distributed subparallel to the deformation flow direction and the {0kl} planes around the shear planes, with preferential alignment of (010) planes in the plane of the foliation (*e.g.* Tommasi *et al.,* 2000; Tommasi and Vauchez, 2015; Demouchy *et al.,* 2023). These CPO symmetries are explained by the dominant activation of {0kl}[100] and (010)[100] dislocation slip systems, and are often referred to as D-type (also known as axial-[100], [100]-fibre, or olivine 'pencil-glide') and A-type olivine fabric in the literature, respectively. Deformation experiments have suggested many microscopic and macroscopic factors to control the olivine CPO patterns in the dislocation creep regime but, among the intrinsic processes acting at the intracrystalline level, the biggest emphasis was put on the role of temperature, confining pressure, differential stress and structurally bonded hydrous defects (*e.g.* Carter and Avé Lallemant, 1970; Durham and Goetze, 1977; Bai *et al.,* 1991; Jung and Karato, 2001; Couvy *et al.,* 2004; Katayama *et al.,* 2004; Raterron *et al.,* 2009, 2011, 2012; Tasaka *et al.,* 2016). In the experimental works of the early 2000s, uncommon olivine fabric types were revealed, which indicated [001] slip direction and/or switches in the common slip plane to (001) or (100). The resulting CPO symmetries were consistent with the dominance of (001)[100], (010)[001] or (100)[001] slip (E-, B- and C-type olivine fabric, respectively), and were suggested to be controlled by the differential stress and the concentration of structurally bonded hydrous defects during deformation (Fig. 7a) (Jung and Karato, 2001; Katayama *et al.*, 2004; Jung *et al.*, 2006; Karato, 2008; Karato *et al.,* 2008). These observations have been used widely to interpret a seismic anisotropy signal in the mantle wedge (*e.g.* Mizukami *et al.,* 2004; Kneller *et al.,* 2005; Katayama and Karato, 2006; Lassak *et al.,* 2006; Tasaka *et al.,* 2008) as well as to render deformation conditions, particularly H_2O content and differential stress, to peridotites displaying a specific olivine CPO symmetry (*e.g.* Karato, 2004). However, considering the saturation of olivine in H_2O at the P-T conditions of experiments (Fig. 7b), large amounts of aqueous fluids were probably present during deformation, which is also corroborated by the published Fourier-Transform Infrared (FTIR) spectra displaying broad bands instead of sharp OH-stretching related peaks (*e.g.* Jung *et al.,* 2006). This suggests that olivine crystals contained the possible maximum of structurally bonded hydrous defects during most of the deformation experiments (Fig. 7b). Hence, apart from a few experiments where olivine may not have reached the saturation (*e.g.* data points in the yellow-shaded field in Fig. 7b), the dependence of olivine CPO types on the concentration of structurally bonded hydrous defects remains ambiguous.

The lack of correlation between structurally bonded H_2O and olivine CPO symmetry is consistent with the results of a recent comprehensive study of olivine CPO types as a function of H_2O content and stresses in natural mantle samples (Bernard *et al.,* 2019). Those authors found that all olivine CPO types were able to form at very low H_2O contents and stresses, and there was no clear relationship between hydrous components in the NAMs and CPO types in natural rocks. The only agreement with experimental results was that A-type olivine CPO symmetry did not occur at H_2O contents above the experimental A-to-E type boundary, and C-type fabric recorded the highest H_2O concentrations (Bernard *et al.,* 2019). However, in the case of the C-type fabric, the effect of pressure in the activation of [001]-directed olivine slip could not be excluded because the corresponding peridotites were garnet-bearing, hence originated at higher-pressure conditions (Bernard *et al.,* 2019). Although structurally bonded hydrous defects in the olivine crystalline lattice possibly have an impact on slip system activity (*e.g.* Tasaka

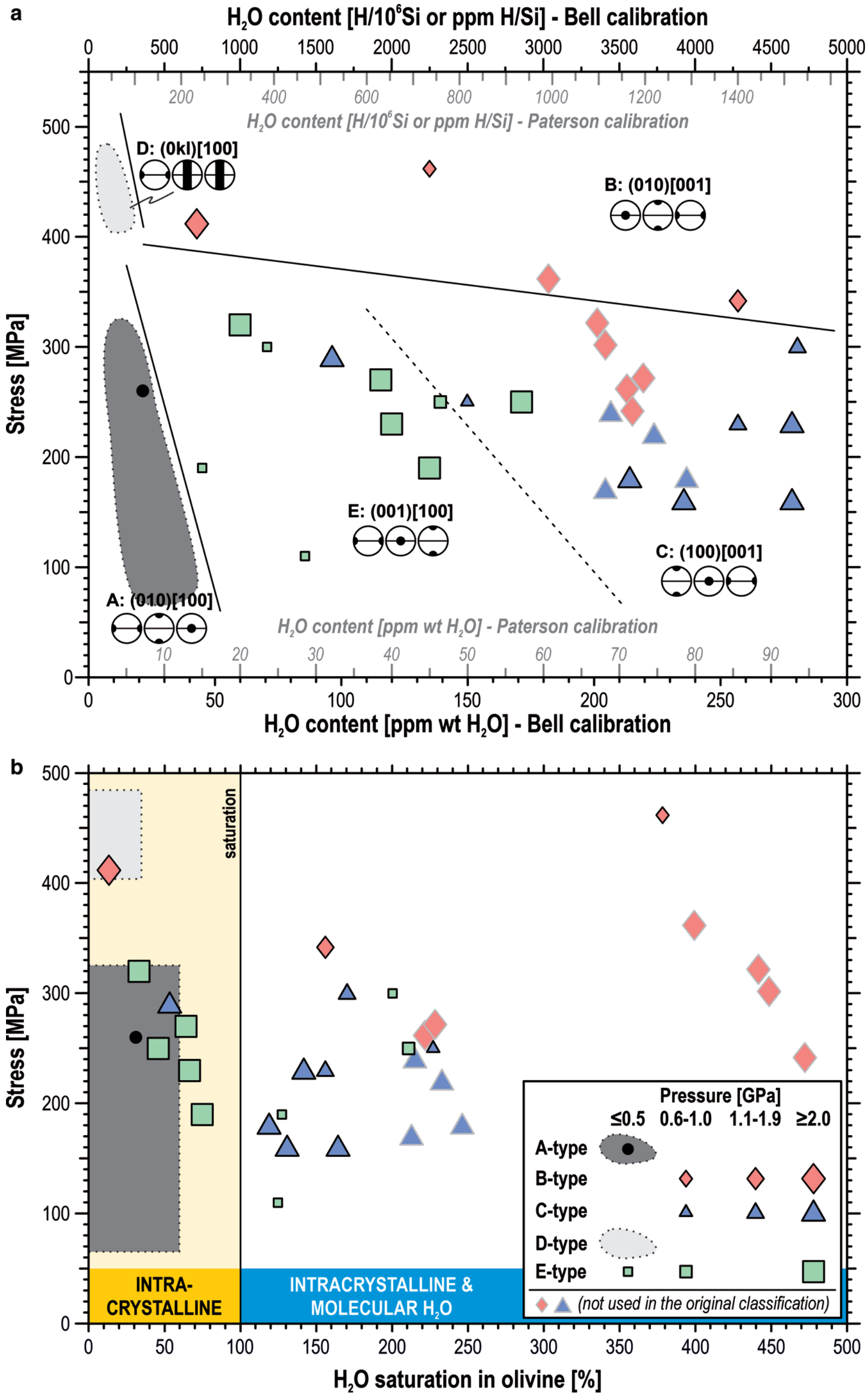
a
H₂O content [H/10⁶Si or ppm H/Si] - Bell calibration
0 500 1000 1500 2000 2500 3000 3500 4000 4500 5000
200 400 600 800 1000 1200 1400
H₂O content [H/10⁶Si or ppm H/Si] - Paterson calibration
D: (0kl)[100]
B: (010)[001]
E: (001)[100]
C: (100)[001]
A: (010)[100]
H₂O content [ppm wt H₂O] - Paterson calibration
10 20 30 40 50 60 70 80 90
Stress [MPa]
0 100 200 300 400 500
0 50 100 150 200 250 300
H₂O content [ppm wt H₂O] - Bell calibration
b
saturation
Stress [MPa]
0 100 200 300 400 500
INTRA-CRYSTALLINE
INTRACRYSTALLINE & MOLECULAR H₂O
Pressure [GPa]
≤0.5 0.6-1.0 1.1-1.9 ≥2.0
A-type
B-type
C-type
D-type
E-type
(not used in the original classification)
0 50 100 150 200 250 300 350 400 450 500
H₂O saturation in olivine [%]

et al., 2016; Faul *et al.,* 2016; Wallis *et al.,* 2019) by altering dislocation self-energy in an anisotropic manner (*e.g.* Karato *et al.,* 2008; Karato, 2013), the natural record indicates that the role of other factors (*e.g.* deformation history, interstitial fluids/melts) in the development of uncommon olivine CPO symmetries in mantle peridotites is significantly larger than that of H_2O concentration and differential stress (*e.g.* Bernard and Behr, 2017; Bernard *et al.,* 2019; Kumamoto *et al.,* 2019). Alternatively, instead of the absolute concentration of hydrous defects bonded in the crystalline structure, it is the incorporation site that may control the microstructural evolution and weakening of H_2O-bearing olivine (Padrón-Navarta *et al.,* 2014, Padrón-Navarta and Hermann, 2017). Recent experimental data are consistent with this hypothesis, suggesting that the type of hydrous defects in olivine and the incorporation site of protons in the crystalline structure coupled to certain trace elements – such as Ti – may influence the hydrolytic weakening of olivine. This influence is pivotal as it ultimately controls the absolute concentration of H_2O under lithospheric conditions when hydrous phases or hydrous melts are not stable (Berry *et al.,* 2005, 2007a,b; Faul *et al.,* 2016). The future direction of research in the field of hydrous weakening of mantle NAMs and the variation of olivine CPO types is thus expected to explore the dependence of rheological behaviour on the incorporation site of structurally bonded protons under truly H_2O-undersaturated conditions.

Fig. 7. (***a***) Variation of olivine crystallographic preferred orientation (CPO) symmetry in the H_2O content [axis at the bottom: ppm wt. H_2O; axis on top: $H/10^6$ Si or ppm H/Si] versus deviatoric stress [MPa] space applied during the high temperature (1100–1300°C) deformation experiments of Bystricky *et al.* (2000), Zhang *et al.* (2000), Jung and Karato (2001), Katayama *et al.* (2004), and Katayama and Karato (2006). The five olivine CPO types (labelled as A-, B-, C-, D- and E-type with a cartoon depicting the corresponding ideal CPO symmetry) are traditionally interpreted as a result of H_2O-induced fabric transitions during dislocation creep deformation (*e.g.* Karato, 2008 and references therein). The schematic cartoons of CPO types are lower hemisphere stereographic projections with the out-of-plane foliation marked by a horizontal solid line. Stretching lineation is at 090°/0° (or 270°/0°) of the pole figures and it develops subparallel to the E–W directed simple shear along the foliation plane; the corresponding dominant dislocation slip system is indicated in the form of (slip plane)[slip direction]. The symbol size of experimental data points is proportional to the confining pressure applied during the deformation experiment; see legend in (**b**). The figure has been modified from Katayama *et al.* (2004); data points with a grey outline were not available at the time the original olivine fabric diagram was published. The H_2O content is adjusted roughly for the Bell *et al.* (2003) calibration, but the method of Paterson (1982) is also provided in grey with italic letters. (***b***) H_2O saturation in olivine [%] versus deviatoric stress [MPa] of the experimental data presented in (**a**). The solubility of H_2O in olivine is calculated following the method of Padrón-Navarta and Hermann (2017) considering TiO_2 concentrations in San Carlos olivine ranging from 12 to 24 ppm wt. TiO_2 (Tollan *et al.,* 2018), and the H_2O saturation in olivine is expressed as the ratio of measured H_2O concentration in olivine (as reported in the original publications, adjusted for the Bell *et al.,* 2003 calibration here) and the theoretical saturation of olivine in H_2O at the pressure-temperature conditions of the corresponding deformation experiments. The 100% saturation (vertical solid line) indicates that all the defects in the olivine crystalline structure are occupied by structurally bonded H_2O, thus further increase in H_2O concentration leads to accommodation of molecular H_2O as visible or invisible fluid inclusions and/or accumulation of excess aqueous fluid at grain boundaries during experiments. Note that most deformation experiments were supersaturated in H_2O (up to ~5×), and the correlation of olivine CPO symmetry type with H_2O content is ambiguous. Only a few high-pressure (>2 GPa) experiments were undersaturated in H_2O, but the concentration of intracrystalline H_2O in olivine in these experiments did not result in the systematic switch of CPO symmetry as suggested by data in (**a**).

2.3. Synkinematic aqueous fluids

Experimental data addressing the effect of synkinematic interstitial aqueous fluids on the rheological behaviour of mantle rocks are scarce. Torsion experiments at 300 MPa and 1200°C on wet olivine polycrystals showed a limited strength decrease by a factor of 2–3 relative to dry samples, which is explained by the presence of both structurally bonded hydrous defects in the olivine structure and importantly by H_2O-derived species in grain boundaries or pores (Demouchy *et al.,* 2012). On the distribution of fluids during ductile deformation, recent high-pressure experiments conducted at 1.2 GPa and 900°C on olivine-pyroxene aggregates have shown that large amounts of aqueous fluids can be concentrated in domains experiencing the highest strain (Précigout *et al.,* 2019). This observation suggests that deformation may enhance fluid pumping into ductile shear zones in the mantle (Précigout *et al.,* 2019), which is primarily driven by dynamically changing pore-fluid pressure at the grain scale during creep cavitation (*e.g.* Fusseis *et al.,* 2009). This potentially has an important feedback on generating shear instabilities, because if melts/fluids can form continuous films at grain boundaries, effective pressure is probably reduced significantly (*e.g.* Karato, 2008). However, unlike interstitial melts, at pressures relevant to the shallow subcontinental upper mantle, H_2O-rich fluids have a large dihedral angle ($\geq$60°) at triple junctions between mineral grains (*e.g.* Watson and Brenan, 1987; Mibe *et al.,* 1999), which impedes efficient wetting of grain boundaries and promotes the formation of fluid pockets instead of interconnected layers, except for very large pore-fluid volumes. Nevertheless, both deformation (*e.g.* Hier-Majumder and Kohlstedt, 2006) and impurities dissolved in the aqueous fluids (*e.g.* Huang *et al.,* 2019; Mysen, 2022) tend to decrease the size of dihedral angles, leading to the formation of interconnected networks of aqueous fluids so that they may reach the base of the crust. If that is the case, the aqueous fluid-saturated grain boundaries – similar to those wetted by interstitial melts (*e.g.* Bai *et al.,* 1997 and references therein) – are expected to serve as a fast intergranular diffusion path. Therefore, free interstitial aqueous fluids may foster the shift of deformation from grain interiors to grain boundaries, favouring fluid-assisted grain boundary migration (*e.g.* Urai *et al.,* 1986) and/or dissolution-precipitation (pressure-solution) creep, which involves advection of elements by the fluid in response to applied stresses (*e.g.* Rutter, 1976; Spiers *et al.,* 2004). This latter deformation mechanism is common in the crust (*e.g.* Wintsch and Yi, 2002; Bestmann *et al.,* 2004) and has also been described in various rock types exhumed from subduction zones (*e.g.* Wassmann and Stöckhert, 2013), but is usually considered to be of minor importance in the deformation of peridotites due to the limited availability of free aqueous fluids in the low-porosity mantle. Nonetheless, experimental data on the solubility of enstatite and forsterite in aqueous fluids at deep lithospheric conditions (700–900°C and 0.4–1.5 GPa; Newton and Manning, 2002) show that silica solubility is sufficient for dissolution-precipitation creep to be efficient during disequilibrium conditions if time-integrated fluid-rock ratios are high. Thus, if free, impure aqueous fluids are present, it is conceivable that dissolution-precipitation creep could equally be a potential deformation mechanism in the shallow lithospheric mantle.

The microstructural record of aqueous fluid-assisted deformation is rare in fresh (*i.e.* non-serpentinized) mantle peridotites. In a plagioclase-facies subcontinental lithospheric mantle peridotite shear zone from the Ronda massif (Spain), Hidas *et al.* (2016) interpreted the progressive strain localization in the presence of synkinematic aqueous fluids during deformation. The shear zone microstructures (*e.g.* crystallization of secondary orthopyroxene in the pressure shadow of porphyroclasts, Fig. 8a) and major element geochemical compositions (*e.g.* no compositional difference between shear-zone rocks and host peridotite) were consistent with dissolution-precipitation creep in a melt-free system. This process is inferred to be responsible for the formation of olivine-rich mylonitic domains alternating with orthopyroxene-rich mylonitic-ultramylonitic bands (Fig. 8a), leaving the modal composition essentially intact at the bulk rock scale, compared to country host peridotites. Moreover, the olivine CPO symmetry recorded a switch from the country host peridotite (axial-[100] or D-type olivine fabric) to the H_2O-impregnated mylonites (so-called E-type olivine fabric) coupled to secondary orthopyroxenes mimicking the olivine CPO within the shear zone (Fig. 8b). This latter observation is inconsistent with dislocation creep deformation of orthopyroxene and indicates oriented crystallization controlled by olivine CPO (Hidas *et al.,* 2016). The origin of the unusual E-type olivine fabric in the plagioclase facies peridotites, however, remained unclear due to the low solubility of hydrous defects in olivine at shallow mantle conditions (<1 GPa; Padrón-Navarta and Hermann, 2017). Nevertheless, from a fossil mantle wedge environment exhumed in the Semail Ophiolite, Oman (Prigent *et al.,* 2018), and from an oceanic transform fault setting (Bickert *et al.,* 2023), similar observations were revealed between porphyroclastic tectonites and intermediate-T (700–900°C) mylonitic-ultramylonitic peridotites, where olivine displayed a remarkable switch to (001)[100] CPO symmetry (*i.e.* E-type olivine fabric) associated with synkinematic oriented crystallization of secondary pyroxenes, mimicking the olivine CPO. Thus, the natural record shows that ductile shear zones can channelize fluid flow in the upper mantle (*e.g.* Précigout *et al.,* 2017, 2019), eventually promoting dissolution-precipitation creep assisted by siliceous fluids (Hidas *et al.,* 2016; Bickert *et al.,* 2023).

The conditions at which dissolution-precipitation may be active in the lithospheric mantle, however, are very limited. This process requires the presence of significant amounts of impure aqueous pore fluids in unaltered mantle, which could be achieved locally in a domain constrained by the upper limit of serpentine and chlorite stability (~750–820°C; *e.g.* Vissers *et al.,* 1995; Padrón-Navarta *et al.,* 2010 and dashed line #2 in Fig. 5a,d in this chapter) and the onset of hydrous melting ($<$1000–1100°C; Green, 1973 and lower limit of free melt domain in Fig. 5a,d in this chapter). So far, the natural record documenting dissolution-precipitation creep in non-altered peridotites is scarce yet these data show that it can be a viable deformation mechanism in the mantle wedge of subduction zones (~700–900°C; Prigent *et al.,* 2018), at oceanic transform faults (~735–945°C; Bickert *et al.,* 2023), and in the shallow subcontinental lithospheric mantle (~750–1000°C; Hidas *et al.,* 2016) (*cf.* Fig. 1), allowing for deformation of peridotites at lower stresses than dislocation creep. If active, dissolution-precipitation creep would imply feedback between deformation and fluid transport and, hence, would promote highly heterogeneous deformation in the shallow upper mantle in diverse

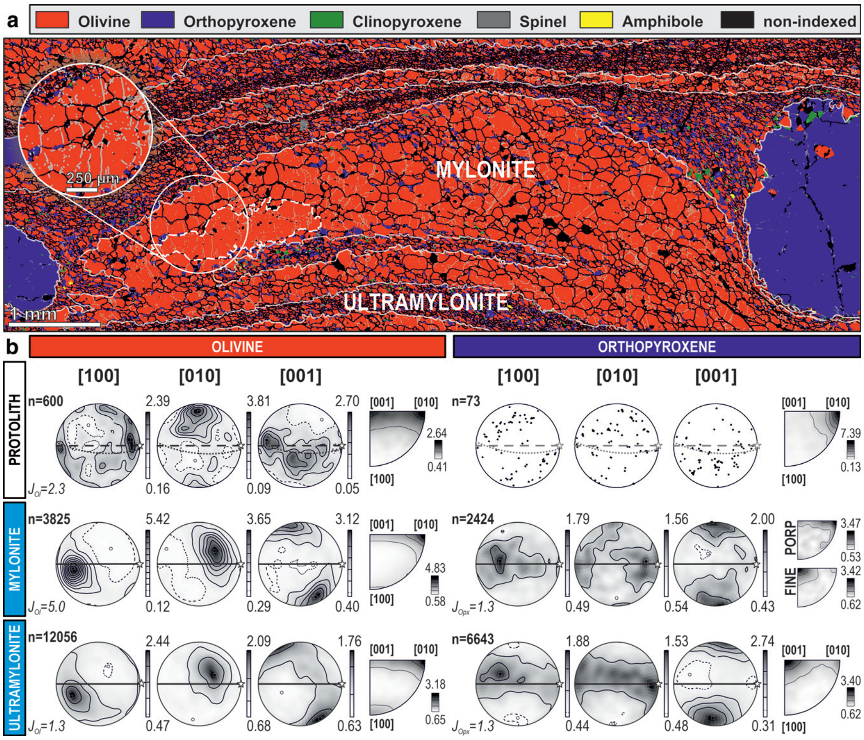

Fig. 8. (***a***) Electron backscatter diffraction (EBSD)-generated phase map of mylonite and ultramylonite microstructures that are interpreted to develop during fluid-assisted ductile strain localization in non-serpentinized peridotites from the Ronda massif (Hidas *et al.,* 2016). The irregular limits between mylonite lenses and ultramylonitic bands are underlined in white. The white dashed line in the mylonite depicts an elongated olivine porphyroclast. Note (i) the corroded grain boundaries of orthopyroxene porphyroclasts and their tails composed of fine-grained, well-mixed olivine-orthopyroxene assemblages that grade into ultramylonitic bands, (ii) the interstitial fine-grained orthopyroxene crystals at the olivine grain boundaries, and (iii) the subgrain boundaries perpendicular to the grain elongation in the inset. The (i) and (ii) are consistent with dissolution-precipitation creep and (iii) indicates activation of dislocation creep in olivine at least in the early stages of deformation. (***b***) Pole figures showing the crystallographic preferred orientation (CPO) of olivine and orthopyroxene in the coarse-grained protolith (microstructure not shown) as well as in the mylonitic and ultramylonitic domains of the shear zone shown in (**a**). The inverse pole figures in the crystal reference frame displaying the rotation axes accommodating low angle (2–15°) misorientations in the two mineral phases are also shown in each microstructural domain. Pole figures are lower hemisphere, equal-area stereographic projections; contours as 0.5 multiples of a uniform distribution; black square: maximum density, white circle: minimum density. Pole figures are plotted using the average orientation of each grain ('one point per grain') to avoid over-representation of large porphyroclasts in the thin sections using the careware software package by David Mainprice. All data are presented in the structural reference frame of the shear zone; the solid horizontal line denotes the average orientation of the foliation and stretching lineation is indicated by a white star. For the protolith, the dashed line indicates the average orientation of the foliation in the shear zone and the dotted line represents the average orientation of the high-T foliation in nearby plagioclase tectonites after Hidas *et al.* (2013). Labels – n: number of measured grains; J_{Ol} and J_{Opx} are the J-indices of olivine and orthopyroxene, respectively, calculated using the MTEX toolbox of MATLAB (https://mtex-toolbox.github.io/, last accessed on 26 October 2023; Bachmann *et al.,*

tectonic settings. Association of highly localized deformation and the very weak olivine CPO produced by dissolution-precipitation creep may also provide an explanation for the very weak seismic anisotropy usually recorded in the fore-arc domains of subduction zones (delay times <0.5 s; *e.g.* Di Leo *et al.,* 2012; Long and Silver, 2008). Altogether, fluid-assisted dissolution-precipitation creep could also be a major rheological process controlling strain localization and faulting at plate boundaries in general (Bickert *et al.,* 2023).

2.4. Fluid-rock interaction at low-*T* deformation

At typical tectonic strain rates (10^{-12} to 10^{-15} s^{-1}), unweathered mantle rocks transition progressively from ductile to semi-brittle behaviour as temperature decreases below ~850–900°C, and they primarily deform by brittle mechanisms below 600°C (*e.g.* Boettcher *et al.,* 2007; Kohli and Warren, 2019; Prigent *et al.,* 2020). In oceanic peridotites, extensive shearing at these low-*T* conditions – yet occurring beyond the serpentinite stability – often produces ultramylonitic shear zones with remarkably fine-grained (<10 μm) minerals, in which strain is predominantly accommodated by grain-size sensitive deformation mechanisms (*e.g.* Jaroslow *et al.,* 1996; Warren and Hirth, 2006). Nevertheless, recent microstructural, petrological and geochemical data indicate that at mid-ocean ridges, the hydrologic cycle might extend past the brittle-ductile transition, and substantial amounts of fluids can reach deep levels of the mantle lithosphere along transform faults (*e.g.* Harigane *et al.,* 2019; Kohli and Warren, 2020; Prigent *et al.,* 2020; Vieira-Duarte *et al.,* 2020; Patterson *et al.,* 2021; Kakihata *et al.,* 2022). Besides ample microstructural evidence for brittle deformation, such as crosscutting intra- and transgranular fractures, as well as pulled apart and/or displaced microboudinage structures, these hydrated low-*T*, non-serpentinized ultramylonites are accompanied by the synkinematic formation of hydrous phases, such as amphibole ± chlorite (*e.g.* Prigent *et al.,* 2020; Vieira-Duarte *et al.,* 2020; Kakihata *et al.,* 2022), and occasionally they may exhibit weak to moderately developed CPO patterns. In such cases, olivine is observed with weak bimodal (010)[001] and (001)[100] CPO symmetries, potentially indicating that low-temperature plasticity was at play under hydrous conditions at high-stress (Kakihata *et al.,* 2022).

At even lower temperatures, provided that H_2O fluid supply is sufficient, and depending on the Si content of the ultramafic rocks (*e.g.* Früh-Green *et al.,* 2004), infiltration along microfractures of the brittle peridotite matrix initiates serpentinization processes, which start with the development of typical mesh textures and culminate in the formation of pure serpentinites at the expense of peridotites (*e.g.* Boudier *et al.,* 2010; Evans *et al.,* 2013; Schwartz *et al.,* 2013; Rouméjon and Cannat, 2014; Rouméjon *et al.,* 2015; Escario *et al.,* 2018). In general, the degree of serpentinization weakens peridotites

---

Fig. 8. *Continued.* 2010; Mainprice *et al.,* 2014); for the interpretation of J-index values, see the caption of Fig. 3. The original version of this figure was published in 'Fluid-assisted strain localization in the shallow subcontinental lithospheric mantle', by Hidas, K., Tommasi, A., Garrido, C.J., Padrón-Navarta, J.A., Mainprice, D., Vauchez, A., Barou, F. and Marchesi, C. (2016) *Lithos,* **262**, 636–650, Copyright Elsevier.

significantly, and it has been shown that slightly serpentinized peridotites have a rheological behaviour similar to that of pure serpentinites (*e.g.* Escartín *et al.,* 2001). Given the high strength of unweathered mantle minerals at low temperatures, serpentinization is expected to promote strain localization in the alteration products, facilitating the development of major (semi-)brittle faults in both subduction zones and oceanic settings. Furthermore, if interstitial fluids accompany such low-T deformation, the deformation is likely to be increasingly accommodated by dissolution and precipitation processes, particularly at the plate interface in subduction zones (*e.g.* Wassmann *et al.,* 2011; Padrón-Navarta *et al.*, 2012; Wassmann and Stöckhert, 2013).

3. Conclusions

In this contribution, we briefly reviewed the effect of different H_2O components on the rheology and microstructural evolution of the upper mantle by contrasting theoretical considerations with available experimental data and the natural record. We recalled that H_2O activity (a_{H_2O}), H_2O fugacity (f_{H_2O}), and H_2O chemical potential (μH_2O) are all related terms but that only μH_2O has a true thermodynamic meaning as it emerges once the stable phases are determined through Gibbs energy minimization. Through thermodynamic calculations in both simple and chemically complex systems, we emphasize that H_2O activity is equal to one only when the system is saturated in H_2O, and this is the only situation in which H_2O fugacity can be computed at any pressure and temperature conditions independently of the bulk amount of H_2O present in the deforming rock. However, under H_2O-saturated conditions, it is more likely that the rheological behaviour of any rock is governed by grain boundary processes rather than the potentially weakening effect of intracrystalline H_2O or the numerical value of f_{H_2O}. Furthermore, available laboratory data and natural observations suggest that:

- The formation of hydrous minerals is very dependent on the whole-rock geochemical composition (*e.g.* availability of Na, K, *etc.*), as well as the prevailing equilibrium pressure and temperature conditions. Consequently, the presence of only small modal amounts (<1–2 vol.%) of these minerals in refractory peridotites at lithospheric mantle conditions is entirely compatible with the percolation of substantial quantities of interstitial aqueous fluids within the rock, as fluids in excess may not lead to an increased crystallization of hydrous phases if other physicochemical conditions in the system are unfavourable. Nevertheless, compared to the dry mantle, the presence of small modal amounts of amphibole indeed implies greater H_2O fugacity and, therefore, larger H_2O contents in NAMs. However, there are situations, such as during mantle exhumation or low-pressure mantle metasomatism, where this expectation is not met. This discrepancy is primarily due to the combination of the low-pressure conditions and, particularly in the case of olivine, the complex behaviour of trace elements in the presence of hydrous phases that limit the potential for the incorporation of extrinsic hydrous defects in the crystalline structure. Overall, small modal amounts of stable hydrous phases and small H_2O

contents in coexisting NAMs in refractory peridotites of the lithospheric mantle cannot be taken as direct evidence of a dry mantle environment.

- Stable, coarse-grained hydrous minerals, such as amphibole and mica, control the H_2O storage capacity of the upper mantle, but their presence alone has little or no impact on the microstructural evolution of their host peridotite during deformation in the dislocation creep regime. Based on natural samples, this observation seems to apply to relatively large modal amounts of such hydrous phases, at least up to 25 vol.%.
- Structurally bonded hydrous defects might weaken rheology, but olivine may not need to be wet to effectively weaken the rheology of the shallow upper mantle.
- Predicted correlation of experimentally deformed olivine CPO-types with H_2O content and stress may not directly apply to nature, where other factors – such as temperature, pressure, deformation mechanism, history and geometry of deformation, strain magnitude and presence of interstitial fluids/melts – play a more significant role in controlling CPO symmetry.
- Synkinematic hydrous or anhydrous melts and aqueous fluids significantly weaken the rheology but their effect is transient, *i.e.* deformation probably remains active as long as a liquid phase is present and it may cease under liquid-absent conditions. This indicates that: (1) in certain tectonic environments (*e.g.* subduction zones, mid-ocean ridges, continental rifts), response of mantle rocks to deformation may be subject to the availability of melts/fluids and, as such, can rapidly change at the geological time-scale; and (2) in these settings the relatively short intermittent periods of active, fluid/melt-assisted deformation may be responsible for the permanent microstructural changes rather than the long periods of tectonic inactivity of the otherwise resistant mantle.
- Interstitial, free aqueous fluids promote potential switches in the dominant deformation slip systems and/or mechanisms, and dissolution-precipitation creep may be a viable deformation mechanism if specific physico-chemical conditions meet in the shallow upper mantle. The presence of synkinematic aqueous fluids, however, is difficult to recognize in most cases because such fluids may not leave an obvious trace in the rock and determining them requires detailed microstructural, petrological and geochemical analyses.
- At low temperatures, but above the stability field of serpentinites, deformation of the upper mantle in the presence of synkinematic H_2O components is progressively dominated by grainsize-sensitive deformation mechanisms, leading to the development of brittle-ductile shear zones that often contain hydrous phases (typically amphibole ± chlorite). Reaching the temperatures of serpentinite stability, H_2O-assisted deformation is essentially controlled by serpentinite minerals, which develop within a resistant matrix composed of original mantle minerals, promoting (semi-)brittle faults and brittle-ductile strain localization at various scales.

We conclude that further experiments and carefully documented natural studies are needed for a better understanding of the effect of the H_2O component on upper mantle rheology. In the future, the role of hydrous volatile species on the microstructural evolution of the mantle must be explored through thermodynamically controlled models, which take into account the availability, speciation, concentration and incorporation into fluids (?) of a wide range of volatile species at different levels of the Earth's deep interior.

Acknowledgements

The authors appreciate the constructive reviews by Marguerite Godard and Alberto Zanetti, as well as the kind assistance and careful editorial work of Costanza Bonadiman and Elisabetta Rampone throughout the writing of this manuscript. José Alberto Padrón-Navarta acknowledges a Ramón y Cajal fellowship (RYC2018-024363-I) funded by the Spanish Ministry of Science and Innovation (MICINN/AEI/10.13039/501100011033) and the FSE program 'FSE invierte en tu futuro', and support by the Junta de Andalucía research project ProyExcel 00757. Károly Hidas acknowledges funding by the Agencia Estatal de Investigación of the MICINN (PID2020-119651RB-I00/AEI/10.13039/501100011033).

References

Aradi, L.E., Hidas, K., Kovács, I.J., Tommasi, A., Klébesz, R., Garrido, C.J. and Szabó, C. (2017) Fluid-enhanced annealing in the subcontinental lithospheric mantle beneath the westernmost margin of the Carpathian–Pannonian extensional basin system. *Tectonics*, **36**, 2987–3011.

Asimow, P.D., Dixon, J.E. and Langmuir, C.H. (2004) A hydrous melting and fractionation model for mid-ocean ridge basalts: Application to the Mid-Atlantic Ridge near the Azores. *Geochemistry, Geophysics, Geosystems*, **5**, Q01E16.

Avé Lallemant, H.G. (1978) Experimental deformation of diopside and websterite. *Tectonophysics*, **48**, 1–27.

Avé Lallemant, H. and Carter, N. (1970) Syntectonic recrystallization of olivine and modes of flow in the upper mantle. *Bulletin of the Geological Society of America*, **81**, 2203–2220.

Bachmann, F., Hielscher, R. and Schaeben, H. (2010) Texture analysis with MTEX - free and open source software toolbox. *Solid State Phenomena*, **160**, 63–68.

Bai, Q., Mackwell, S.J. and Kohlstedt, D.L. (1991) High-Temperature Creep of Olivine Single-Crystals. 1. Mechanical Results for Buffered Samples. *Journal of Geophysical Research–Solid Earth and Planets*, **96**, 2441–2463.

Bai, Q., Jin, Z.-M. and Green, H.W. (1997) Experimental investigation of the rheology of partially molten peridotite at upper mantle pressures and temperatures. Pp. 40–61 in: *Deformation-enhanced Fluid Transport in the Earth's Crust and Mantle* (M.B. Holness, editor). Chapman & Hall, London.

Bell, D.R., Rossman, G.R., Maldener, J., Endisch, D. and Rauch, F. (2003) Hydroxide in olivine: A quantitative determination of the absolute amount and calibration of the IR spectrum. *Journal of Geophysical Research–Solid Earth*, **108**, No. B2, 2105, https://dx.doi.org/10.1029/2001JB000679.

Bernard, R.E. and Behr, W.M. (2017) Fabric heterogeneity in the Mojave lower crust and lithospheric mantle in Southern California. *Journal of Geophysical Research: Solid Earth*, **122**, 5000–5025.

Bernard, R.E., Behr, W.M., Becker, T.W. and Young, D.J. (2019) Relationships between olivine CPO and deformation parameters in naturally deformed rocks and implications for mantle seismic anisotropy. *Geochemistry, Geophysics, Geosystems*, **20**, 3469–3494.

Berry, A.J., Hermann, J., O'Neill, H.S.C. and Foran, G.J. (2005) Fingerprinting the water site in mantle olivine. *Geology,* **33**, 869–872.

Berry, A.J., O'Neill, H.S.C., Hermann, J. and Scott, D.R. (2007a) The infrared signature of water associated with trivalent cations in olivine. *Earth and Planetary Science Letters,* **261**, 134–142.

Berry, A.J., Walker, A.M., Hermann, J., O'Neill, H.S.C., Foran, G.J. and Gale, J.D. (2007b) Titanium substitution mechanisms in forsterite. *Chemical Geology,* **242**, 176–186.

Bestmann, M., Prior, D.J. and Veltkamp, K.T.A. (2004) Development of single-crystal σ-shaped quartz porphyroclasts by dissolution-precipitation creep in a calcite marble shear zone. *Journal of Structural Geology*, **26**, 869–883.

Bickert, M., Kaczmarek, M.-A., Brunelli, D., Maia, M., Campos, T.F.C. and Sichel, S.E. (2023) Fluid-assisted grain size reduction leads to strain localization in oceanic transform faults. *Nature Communications*, **14**, 4087.

Blacic, J.D. (1975) Plastic-deformation mechanisms in quartz: The effect of water. *Tectonophysics*, **27**, 271–294.

Boettcher, M.S., Hirth, G., Evans, B. (2007) Olivine friction at the base of oceanic seismogenic zones. *Journal of Geophysical Research: Solid Earth*, **112**, B01205.

Boioli, F., Tommasi, A., Cordier, P., Demouchy, S. and Mussi, A. (2015) Low steady-state stresses in the cold lithospheric mantle inferred from dislocation dynamics models of dislocation creep in olivine. *Earth and Planetary Science Letters*, **432**, 232–242.

Bonadiman, C., Brombin, V., Andreozzi, G.B., Benna, P., Coltorti, M., Curetti, N., Faccini, B., Merli, M., Pelorosso, B., Stagno, V., Tesauro, M. and Pavese, A. (2021) Phlogopite-pargasite coexistence in an oxygen reduced spinel-peridotite ambient. *Scientific Reports*, **11**, 11829.

Boudier, F., Baronnet, A. and Mainprice, D. (2010) Serpentine mineral replacements of natural olivine and their seismic implications: oceanic lizardite versus subduction-related antigorite. *Journal of Petrology*, **51**, 495–512.

Bunge, H.J. (1982) *Texture Analysis in Materials Science*. Butterworth, London, 593 pp.

Bureau, H. and Keppler, H. (1999) Complete miscibility between silicate melts and hydrous fluids in the upper mantle: experimental evidence and geochemical implications. *Earth and Planetary Science Letters*, **165**, 187–196.

Bürgmann, R. and Dresen, G. (2008) Rheology of the Lower Crust and Upper Mantle: Evidence from Rock Mechanics, Geodesy, and Field Observations. *Annual Review of Earth and Planetary Sciences*, **36**, 531–567.

Bystricky, M., Kunze, K., Burlini, L. and Burg, J.P. (2000) High shear strain of olivine aggregates; rheological and seismic consequences. *Science*, **290**, 1564–1567.

Carter, N. and Avé Lallemant, H. (1970) High temperature flow of dunite and peridotite. *Bulletin of the Geological Society of America*, **81**, 2181–2202.

Chen, S., Hiraga, T. and Kohlstedt, D.L. (2006) Water weakening of clinopyroxene in the dislocation creep regime. *Journal of Geophysical Research*, **111**, B08203, https://dx.doi.org/10.1029/2005JB003885.

Coltorti, M., Bonadiman, C., Faccini, B., Gregoire, M., O'Reilly, S.Y. and Powell, W. (2007) Amphiboles from suprasubduction and intraplate lithospheric mantle. *Lithos*, **99**, 68–84.

Connolly, J.A.D. (2009) The geodynamic equation of state: What and how. *Geochemistry Geophysics Geosystems*, **10**, Q10014.

Connolly, J.A.D. and Kerrick, D.M. (1987) An algorithm and computer-program for calculating composition phase-diagrams. *CALPHAD*, **11**, 1–55.

Couvy, H., Frost, D., Heidelbach, F., Nyilas, K., Ungár, T., Mackwell, S. and Cordier, P. (2004) Shear deformation experiments of forsterite at 11 GPa-1400°C in the multianvil apparatus. *European Journal of Mineralogy*, **16**, 877–889.

Dawson, J.B. and Smith, J.V. (1982) Upper mantle amphiboles: a review. *Mineralogical Magazine*, **45**, 35–46.

Demouchy, S. and Tommasi, A. (2021) From dry to damp and stiff mantle lithosphere by reactive melt percolation atop the Hawaiian plume. *Earth and Planetary Science Letters,* **574**, 117159.

Demouchy, S., Tommasi, A., Barou, F., Mainprice, D. and Cordier, P. (2012) Deformation of olivine in torsion under hydrous conditions. *Physics of the Earth and Planetary Interiors*, **202**, 56–70.

Demouchy, S., Tommasi, A., Ballaran, T.B. and Cordier, P. (2013) Low strength of Earth's uppermost mantle inferred from tri-axial deformation experiments on dry olivine crystals. *Physics of the Earth and Planetary Interiors*, **220**, 37–49.

Demouchy, S., Mussi, A., Barou, F., Tommasi, A. and Cordier, P. (2014) Viscoplasticity of polycrystalline olivine experimentally deformed at high pressure and 900°C. *Tectonophysics*, **623**, 123–135.

Demouchy, S., Wang, Q. and Tommasi, A. (2023) Deforming the upper mantle — Olivine mechanical properties and anisotropy. *Elements*, **19**, 151–157.

Denis, C.M.M., Alard, O. and Demouchy, S. (2015) Water content and hydrogen behaviour during metasomatism in the uppermost mantle beneath Ray Pic volcano (Massif Central, France). *Lithos*, **236–237**, 256–274.

Di Leo, J.F., Wookey, J., Hammond, J.O.S., Kendall, J.M., Kaneshima, S., Inoue, H., Yamashina, T. and Harjadi, P. (2012) Deformation and mantle flow beneath the Sangihe subduction zone from seismic anisotropy. *Physics of the Earth and Planetary Interiors*, **194–195**, 38–54.

Durham, W.B. and Goetze, C. (1977) Plastic flow of oriented single crystals of olivine: 1. Mechanical data. *Journal of Geophysical Research*, **82**, 5737–5753.

Escario, S., Godard, M., Gouze, P. and Leprovost, R. (2018) Experimental study of the effects of solute transport on reaction paths during incipient serpentinization. *Lithos*, **323**, 191–207.

Escartín, J., Hirth, G., Evans, B. (2001) Strength of slightly serpentinized peridotites: Implications for the tectonics of oceanic lithosphere. *Geology*, **29**, 1023-1026.

Evans, B.W., Hattori, K. and Baronnet, A. (2013) Serpentinite: what, why, where? *Elements*, **9**, 99–106.

Faul, U.H., Cline Ii, C.J., David, E.C., Berry, A.J. and Jackson, I. (2016) Titanium-hydroxyl defect-controlled rheology of the Earth's upper mantle. *Earth and Planetary Science Letters*, **452**, 227–237.

Fei, H., Wiedenbeck, M., Yamazaki, D. and Katsura, T. (2013) Small effect of water on upper-mantle rheology based on silicon self-diffusion coefficients. *Nature*, **498**, 213–215.

Früh-Green, G.L., Connolly, J.A.D., Plas, A., Kelley, D.S. and Grobéty, B. (2004) Serpentinization of oceanic peridotites: implications for geochemical cycles and biological activity. Pp. 119–136 in: *The Subseafloor Biosphere at Mid-Ocean Ridges* (W.S.D. Wilcock, E.F. Delong, D.S. Kelley, J.A. Baross and S.C. Cary, editors). Geophysical Monograph Series. American Geophysical Union.

Fumagalli, P. and Klemme, S. (2015) 2.02 – Mineralogy of the Earth: Phase Transitions and Mineralogy of the Upper Mantle. Pp. 7–31 in: *Treatise on Geophysics* (2nd edition). Elsevier, Oxford, UK.

Fusseis, F., Regenauer-Lieb, K., Liu, J., Hough, R.M. and De Carlo, F. (2009) Creep cavitation can establish a dynamic granular fluid pump in ductile shear zones. *Nature*, **459**, 974–977.

Girard, J., Chen, J., Raterron, P. and Holyoke, C.W. (2013) Hydrolytic weakening of olivine at mantle pressure: Evidence of [100](010) slip system softening from single-crystal deformation experiments. *Physics of the Earth and Planetary Interiors*, **216**, 12–20.

Green, D.H. (1973) Experimental melting studies on a model upper mantle composition at high pressure under water-saturated and water-undersaturated conditions. *Earth and Planetary Science Letters*, **19**, 37–53.

Green, D.H. (2015) Experimental petrology of peridotites, including effects of water and carbon on melting in the Earth's upper mantle. *Physics and Chemistry of Minerals*, **42**, 95–122.

Green, D.H., Hibberson, W.O., Kovács, I. and Rosenthal, A. (2010) Water and its influence on the lithosphere-asthenosphere boundary. *Nature*, **467**, 448–451.

Greenwood, H.J. (1961) The system $NaAlSi_2O_6$-H_2O-argon: Total pressure and water pressure in metamorphism. *Journal of Geophysical Research (1896–1977)*, **66**, 3923–3946.

Griggs, D. (1967) Hydrolytic weakening of quartz and other silicates. *Geophysical Journal of the Royal Astronomical Society*, **14**, 19–31.

Griggs, D.T. and Blacic, J.D. (1965) Quartz: anomalous weakness of synthetic crystals. *Science*, **147**, 292–295.

Hansen, L.N., Faccenda, M. and Warren, J.M. (2021) A review of mechanisms generating seismic anisotropy in the upper mantle. *Physics of the Earth and Planetary Interiors*, **313**, 106662.

Hao, Y.-T., Xia, Q.-K., Tian, Z.-Z. and Liu, J. (2016) Mantle metasomatism did not modify the initial H_2O content in peridotite xenoliths from the Tianchang basalts of eastern China. *Lithos*, **260**, 315–327.

Harigane, Y., Okamoto, A., Morishita, T., Snow, J.E., Tamura, A., Yamashita, H., Michibayashi, K., Ohara, Y. and Arai, S. (2019) Melt–fluid infiltration along detachment shear zones in oceanic core complexes: Insights from amphiboles in gabbro mylonites from the Godzilla Megamullion, Parece Vela Basin, the Philippine Sea. *Lithos*, **344–345**, 217–231.

Hermann, J., Spandler, C., Hack, A. and Korsakov, A.V. (2006) Aqueous fluids and hydrous melts in high-pressure and ultra-high pressure rocks: Implications for element transfer in subduction zones. *Lithos*, **92**, 399–417.

Hidas, K., Booth-Rea, G., Garrido, C.J., Martínez-Martínez, J.M., Padrón-Navarta, J.A., Konc, Z., Giaconia, F., Frets, E. and Marchesi, C. (2013) Backarc basin inversion and subcontinental mantle emplacement in the crust: kilometre-scale folding and shearing at the base of the proto-Alborán lithospheric mantle (Betic Cordillera, southern Spain). *Journal of the Geological Society, London*, **170**, 47–55.

Hidas, K., Tommasi, A., Garrido, C.J., Padrón-Navarta, J.A., Mainprice, D., Vauchez, A., Barou, F. and Marchesi, C. (2016) Fluid-assisted strain localization in the shallow subcontinental lithospheric mantle. *Lithos*, **262**, 636–650.

Hier-Majumder, S. and Kohlstedt, D.L. (2006) Role of dynamic grain boundary wetting in fluid circulation beneath volcanic arcs. *Geophysical Research Letters*, **33**.

Higgie, K. and Tommasi, A. (2012) Feedbacks between deformation and melt distribution in the crust-mantle transition zone of the Oman ophiolite. *Earth and Planetary Science Letters*, **359**, 61–72.

Higgie, K. and Tommasi, A. (2014) Deformation in a partially molten mantle: Constraints from plagioclase lherzolites from Lanzo, western Alps. *Tectonophysics*, **615**, 167–181.

Hirth, G. and Kohlstedt, D.L. (1995a) Experimental constraints on the dynamics of the partially molten upper-mantle – Deformation in the diffusion creep regime. *Journal of Geophysical Research – Solid Earth*, **100**, 1981–2001.

Hirth, G. and Kohlstedt, D.L. (1995b) Experimental constraints on the dynamics of the partially molten upper-mantle – Deformation in the dislocation creep regime. *Journal of Geophysical Research – Solid Earth*, **100**, 15441–15449.

Hirth, G. and Kohlstedt, D.L. (1996) Water in the oceanic upper mantle: Implications for rheology, melt extraction and the evolution of the lithosphere. *Earth and Planetary Science Letters*, **144**, 93–108.

Hirth, G. and Kohlstedt, D. (2003) Rheology of the upper mantle and the mantle wedge: a view from the experimentalists. Pp. 83–105 in: *Inside the Subduction Factory* (J.M. Eiler, editor). Geophysical Monograph, American Geophysical Union, San Francisco, USA.

Holland, T.J.B. and Powell, R. (2011) An improved and extended internally consistent thermodynamic dataset for phases of petrological interest, involving a new equation of state for solids. *Journal of Metamorphic Geology*, **29**, 333–383.

Holland, T.J.B., Green, E.C.R. and Powell, R. (2018) Melting of Peridotites through to Granites: A Simple Thermodynamic Model in the System KNCFMASHTOCr. *Journal of Petrology*, **59**, 881–900.

Holtzman, B.K., Groebner, N.J., Zimmerman, M.E., Ginsberg, S.B. and Kohlstedt, D.L. (2003a) Stress-driven melt segregation in partially molten rocks. *Geochemistry Geophysics Geosystems*, **4**, art. no.-8607.

Holtzman, B.K., Kohlstedt, D.L., Zimmerman, M.E., Heidelbach, F., Hiraga, T. and Hustoft, J. (2003b) Melt segregation and strain partitioning: Implications for seismic anisotropy and mantle flow. *Science*, **301**, 1227–1230.

Huang, Y., Nakatani, T., Nakamura, M. and McCammon, C. (2019) Saline aqueous fluid circulation in mantle wedge inferred from olivine wetting properties. *Nature Communications*, **10**, 5557.

Jaroslow, G.E., Hirth, G. and Dick, H.J.B. (1996) Abyssal peridotite mylonites: implications for grain-size sensitive flow and strain localization in the oceanic lithosphere. *Tectonophysics*, **256**, 17–37.

Jollands, M.C., Dohmen, R. and Padrón-Navarta, J.A. (2023) Hide and seek — Trace element incorporation and diffusion in olivine. *Elements*, **19**, 144–150.

Jung, H. and Karato, S.-I. (2001) Water-induced fabric transitions in olivine. *Science*, **293**, 1460–1463.

Jung, H., Katayama, I., Jiang, Z., Hiraga, I. and Karato, S. (2006) Effect of water and stress on the lattice-preferred orientation of olivine. *Tectonophysics*, **421**, 1-22.

Kakihata, Y., Michibayashi, K. and Dick, H.J.B. (2022) Heterogeneity in texture and crystal fabric of intensely hydrated ultramylonitic peridotites along a transform fault, Southwest Indian Ridge. *Tectonophysics*, **823**, 229206.

Karato, S.-I. (2004) Mapping water content in the upper mantle. Pp. 135–152 in: *Inside the Subduction Factory* (J. Eiler, editor). Geophysical Monograph Series, **138**, American Geophysical Union, Washington, D.C.

Karato, S.-I. (2008) *Deformation of Earth materials: An Introduction to the Rheology of Solid Earth*. Cambridge University Press, Cambridge, New York, 463 pp.

Karato, S.-I. (2010) Rheology of the Earth's mantle: A historical review. *Gondwana Research*, **18**, 17–45.

Karato, S.-I. (2013) *Rheological Properties of Minerals and Rocks. Physics and Chemistry of the Deep Earth.* John Wiley & Sons, Ltd, pp. 94–144.

Karato, S.-I. and Jung, H. (2003) Effects of pressure on high-temperature dislocation creep in olivine. *Philosophical Magazine*, **83**, 401–414.

Karato, S.-I. and Wu, P. (1993) Rheology of the Upper Mantle: A Synthesis. *Science*, **260**, 771–778.

Karato, S.-I., Jung, H., Katayama, I. and Skemer, P. (2008) Geodynamic significance of seismic anisotropy of the upper mantle: New insights from laboratory studies. *Annual Review of Earth and Planetary Sciences*, **36**, 59–95.

Katayama, I. and Karato, S.-I. (2006) Effect of temperature on the B- to C-type olivine fabric transition and implication for flow pattern in subduction zones. *Physics of The Earth and Planetary Interiors*, **157**, 33–45.

Katayama, I., Jung, H. and Karato, S.-I. (2004) New type of olivine fabric from deformation experiments at modest water content and low stress. *Geology*, **32**, 1045–1048.

King, D.S.H., Zimmerman, M.E. and Kohlstedt, D.L. (2010) Stress-driven Melt Segregation in Partially Molten Olivine-rich Rocks Deformed in Torsion. *Journal of Petrology*, **51**, 21–42.

Klemme, S. and Stalder, R. (2018) Halogens in the Earth's mantle: What we know and what we don't. Pp. 847–869 in: *The Role of Halogens in Terrestrial and Extraterrestrial Geochemical Processes: Surface, Crust, and Mantle* (D.E. Harlov and L. Aranovich, editors). Springer International Publishing.

Kneller, E.A., van Keken, P.E., Karato, S.-I. and Park, J. (2005) B-type olivine fabric in the mantle wedge: Insights from high-resolution non-Newtonian subduction zone models. *Earth and Planetary Science Letters*, **237**, 781–797.

Kohli, A.H. and Warren, J.M. (2020) Evidence for a deep hydrologic cycle on oceanic transform faults. *Journal of Geophysical Research: Solid Earth*, **125**, e2019JB017751.

Kohlstedt, D.L. and Hansen, L.N. (2015) Constitutive equations, rheological behavior, and viscosity of rocks. Pp. 441–472 in: *Treatise on Geophysics* (2nd edition). (G. Schubert, editor). Elsevier, Amsterdam.

Kohlstedt, D.L. and Zimmerman, M.E. (1996) Rheology of partially molten mantle rocks. *Annual Review of Earth and Planetary Sciences*, **24**, 41–62.

Kohlstedt, D.L., Evans, B. and Mackwell, S.J. (1995) Strength of the lithosphere - Constraints imposed by laboratory experiments. *Journal of Geophysical Research – Solid Earth*, **100**, 17587–17602.

Kohlstedt, D.L., Zimmerman, M.E. and Mackwell, S.J. (2010) Stress-driven melt segregation in partially molten feldspathic rocks. *Journal of Petrology*, **51**, 9–19.

Konzett, J. and Ulmer, P. (1999) The stability of hydrous potassic phases in lherzolitic mantle – An experimental study to 9.5 GPa in simplified and natural bulk compositions. *Journal of Petrology*, **40**, 629–652.

Kovács, I.J., Liptai, N., Koptev, A., Cloetingh, S.A.P.L., Lange, T.P., Matenco, L., Szakács, A., Radulian, M., Berkesi, M., Patkó, L., Molnár, G., Novák, A., Wesztergom, V., Szabó, Cs. and Fancsik, T. (2021) The 'pargasosphere' hypothesis: Looking at global plate tectonics from a new perspective. *Global and Planetary Change*, **204**, 103547.

Kumamoto, K.M., Warren, J.M. and Hansen, L.N. (2019) Evolution of the Josephine Peridotite shear zones: 2. Influences on olivine CPO evolution. *Journal of Geophysical Research: Solid Earth*, **124**, 12763–12781.

Lassak, T.M., Fouch, M.J., Hall, C.E. and Kaminski, É. (2006) Seismic characterization of mantle flow in subduction systems: Can we resolve a hydrated mantle wedge? *Earth and Planetary Science Letters*, **243**, 632–649.

Long, M.D. and Silver, P.G. (2008) The Subduction Zone Flow Field from Seismic Anisotropy: A Global View. *Science*, **319**, 315–318.

Mainprice, D., Bachmann, F., Hielscher, R. and Schaeben, H. (2014) Descriptive tools for the analysis of texture projects with large datasets using MTEX: strength, symmetry and components. Special Publications, **409,** Geological Society, London.

Mainprice, D., Barruol, G. and Ben Ismaïl, W. (2000) The seismic anisotropy of the Earth's mantle: from single crystal to polycrystal. Pp. 237–264 in: *Earth's Deep Interior: Mineral Physics and Tomography from the Atomic to the Global Scale* (S.I. Karato, editor). Geodynamics Series, AGU, Washington, D.C.

Mandler, B.E. and Grove, T.L. (2016) Controls on the stability and composition of amphibole in the Earth's mantle. *Contributions to Mineralogy and Petrology*, **171**, 68.

Manning, C.E. (2004a) The chemistry of subduction-zone fluids. *Earth and Planetary Science Letters*, **223**, 1–16.

Manning, C.E. (2004b) Polymeric silicate complexing in aqueous fluids at high pressure and temperature, and its implications for water-rock interaction. Pp. 45–49 in: *Water–Rock Interaction* (R.B. Wanty and R.R. Seal, II, editors). Taylor & Francis Group, London.

Mei, S. and Kohlstedt, D.L. (2000a) Influence of water on plastic deformation of olivine aggregates: 1. Diffusion creep regime. *Journal of Geophysical Research: Solid Earth*, **105**, 21457–21469.

Mei, S. and Kohlstedt, D.L. (2000b) Influence of water on plastic deformation of olivine aggregates: 2. Dislocation creep regime. *Journal of Geophysical Research: Solid Earth*, **105**, 21471–21481.

Mei, S., Bai, W., Hiraga, T. and Kohlstedt, D.L. (2002) Influence of melt on the creep behavior of olivine-basalt aggregates under hydrous conditions. *Earth and Planetary Science Letters*, **201**, 491–507.

Melekhova, E., Schmidt, M.W., Ulmer, P. and Pettke, T. (2007) The composition of liquids coexisting with dense hydrous magnesium silicates at 11–13.5 GPa and the endpoints of the solidi in the MgO–SiO_2–H_2O system. *Geochimica et Cosmochimica Acta*, **71**, 3348–3360.

Mengel, K. and Green, D.H. (1989) Stability of amphibole and phlogopite in metasomatized peridotite under water-saturated and water-undersaturated conditions. Pp. 571–581 in: *Fourth International Kimberlite Conference, Perth* (J. Ross, editor). Special Publication, Geological Society of America, Boulder, Colorado, USA.

Mibe, K., Fujii, T. and Yasuda, A. (1999) Control of the location of the volcanic front in island arcs by aqueous fluid connectivity in the mantle wedge. *Nature*, **401**, 259–262.

Mibe, K., Kanzaki, M., Kawamoto, T., Matsukage, K.N., Fei, Y. and Ono, S. (2007) Second critical endpoint in the peridotite-H_2O system. *Journal of Geophysical Research: Solid Earth*, **112**, B03201.

Mizukami, T., Wallis, S.R. and Yamamoto, J. (2004) Natural examples of olivine lattice preferred orientation patterns with a flow-normal a-axis maximum. *Nature*, **427**, 432–436.

Mysen, B. (2022) Fluids and physicochemical properties and processes in the Earth. *Progress in Earth and Planetary Science*, **9**, 54.

Newton, R.C. and Manning, C.E. (2002) Experimental determination of calcite solubility in H_2O-NaCl solutions at deep crust/upper mantle pressures and temperatures: Implications for metasomatic processes in shear zones. *American Mineralogist*, **87**, 1401–1409.

O'Reilly, S. and Griffin, W.L. (2013) *Mantle Metasomatism, Metasomatism and the Chemical Transformation of Rock*. Springer Berlin Heidelberg, pp. 471–533.

Otsuka, K. and Karato, S.-I. (2011) Control of the water fugacity at high pressures and temperatures: Applications to the incorporation mechanisms of water in olivine. *Physics of the Earth and Planetary Interiors*, **189**, 27–33.

Padrón-Navarta, J.A. (2019) Phase diagrams for Nominally Anhydrous Minerals, Goldschmidt2019. *Goldschmidt Abstracts*, Barcelona, Spain, p. 2548.

Padrón-Navarta, J.A. and Hermann, J. (2017) A subsolidus olivine water solubility equation for the Earth's upper mantle. *Journal of Geophysical Research: Solid Earth*, **122**, 9862–9880.

Padrón-Navarta, J.A., Tommasi, A., Garrido, C.J., López Sánchez-Vizcaíno, V. (2012). Plastic deformation and development of antigorite crystal preferred orientation in high-pressure serpentinites. *Earth and Planetary Science Letters*, **349–350**, 75–86.

Padrón-Navarta, J.A., Hermann, J., Garrido, C.J., López Sánchez-Vizcaíno, V. and Gómez-Pugnaire, M.T. (2010) An experimental investigation of antigorite dehydration in natural silica-enriched serpentinite. *Contributions to Mineralogy and Petrology*, **159**, 25–42.

Padrón-Navarta, J.A., Hermann, J. and O'Neill, H.S.C. (2014) Site-specific hydrogen diffusion rates in forsterite. *Earth and Planetary Science Letters*, **392**, 100–112.

Paterson, M.S. (1982) The determination of hydroxyl by infrared absorption in quartz, silicate glasses and similar materials. *Bulletin de Minéralogie*, **105**, 20–29.

Patterson, S.N., Lynn, K.J., Prigent, C. and Warren, J.M. (2021) High temperature hydrothermal alteration and amphibole formation in Gakkel Ridge abyssal peridotites. *Lithos*, **392–393**, 106107.

Pitzer, K.S. and Sterner, S.M. (1994) Equations of state valid continuously from zero to extreme pressures for H_2O and CO_2. *Journal of Chemical Physics*, **101**, 3111–3116.

Powell, R., Evans, K.A., Green, E.C.R. and White, R.W. (2019) The truth and beauty of chemical potentials. *Journal of Metamorphic Geology*, **37**, 1007–1019.

Précigout, J., Prigent, C., Palasse, L. and Pochon, A. (2017) Water pumping in mantle shear zones. *Nature Communications*, **8**, 15736.

Précigout, J., Stünitz, H. and Villeneuve, J. (2019) Excess water storage induced by viscous strain localization during high-pressure shear experiment. *Scientific Reports*, **9**, 3463.

Prigent, C., Guillot, S., Agard, P. and Ildefonse, B. (2018) Fluid-Assisted Deformation and Strain Localization in the Cooling Mantle Wedge of a Young Subduction Zone (Semail Ophiolite). *Journal of Geophysical Research: Solid Earth*, **123**, 7529–7549.

Prigent, C., Warren, J.M., Kohli, A.H. and Teyssier, C. (2020) Fracture-mediated deep seawater flow and mantle hydration on oceanic transform faults. *Earth and Planetary Science Letters*, **532**, 115988.

Raterron, P., Amiguet, E., Chen, J., Li, L. and Cordier, P. (2009) Experimental deformation of olivine single crystals at mantle pressures and temperatures. *Physics of The Earth and Planetary Interiors*, **172**, 74–83.

Raterron, P., Chen, J., Geenen, T. and Girard, J. (2011) Pressure effect on forsterite dislocation slip systems: Implications for upper-mantle LPO and low viscosity zone. *Physics of the Earth and Planetary Interiors*, **188**, 26–36.

Raterron, P., Girard, J. and Chen, J. (2012) Activities of olivine slip systems in the upper mantle. *Physics of the Earth and Planetary Interiors*, **200-201**, 105–112.

Rouméjon, S. and Cannat, M. (2014) Serpentinization of mantle-derived peridotites at mid-ocean ridges: Mesh texture development in the context of tectonic exhumation. *Geochemistry, Geophysics, Geosystems*, **15**, 2354 – 2379.

Rouméjon, S., Cannat, M., Agrinier, P., Godard, M. and Andreani, M. (2015) Serpentinization and fluid pathways in tectonically exhumed peridotites from the Southwest Indian Ridge (62–65°E). *Journal of Petrology*, **56**, 703–734.

Rutter, E.H. (1976) The kinetics of rock deformation by pressure solution. *Philosophical Transactions of the Royal Society of London*, **A283**.

Schwartz, S., Guillot, S., Reynard, B., Lafay, R., Debret, B., Nicollet, C., Lanari, P. and Auzende, A.L. (2013) Pressure–temperature estimates of the lizardite/antigorite transition in high pressure serpentinites. *Lithos*, **178**, 197–210.

Scott, T. and Kohlstedt, D.L. (2006). The effect of large melt fraction on the deformation behavior of peridotite. *Earth and Planetary Science Letters*, **246**, 177–187.

Shaw, C.S.J. (2009) Textural development of amphibole during breakdown reactions in a synthetic peridotite. *Lithos*, **110**, 215–228.

Soustelle, V., Tommasi, A., Demouchy, S. and Ionov, D.A. (2010) Deformation and Fluid–Rock Interaction in the Supra-subduction Mantle: Microstructures and Water Contents in Peridotite Xenoliths from the Avacha Volcano, Kamchatka. *Journal of Petrology*, **51**, 363–394.

Soustelle, V., Walte, N.P., Manthilake, M.A.G.M. and Frost, D.J. (2014) Melt migration and melt-rock reactions in the deforming Earth's upper mantle: Experiments at high pressure and temperature. *Geology*, **42**, 83–86.

Spear, F.S. (1995) *Metamorphic Phase Equilibria and Pressure-temperature-time Paths*. Mineralogical Society of America, Washington, D.C., 799 pp.

Spiers, C.J., De Meer, S., Niemeijer, A.R. and Zhang, X. (2004) Kinetics of rock deformation by pressure solution and the role of thin aqueous films. Pp. 129–158 in: *Physicochemistry of Water in Geological and Biological Systems: Structures and Properties of Thin Aqueous Films* (S. Nakashima, C.J. Spiers, L. Mercury, P.A. Fenter and M.F. Hocheller, editors). Universal Academy Press, Inc., Tokyo.

Takei, Y. and Holtzman, B.K. (2009a) Viscous constitutive relations of solid-liquid composites in terms of grain boundary contiguity: 1. Grain boundary diffusion control model. *Journal of Geophysical Research: Solid Earth*, **114**, B06205.

Takei, Y. and Holtzman, B.K. (2009b) Viscous constitutive relations of solid-liquid composites in terms of grain boundary contiguity: 2. Compositional model for small melt fractions. *Journal of Geophysical Research: Solid Earth*, **114**, B06206.

Takei, Y. and Holtzman, B.K. (2009c) Viscous constitutive relations of solid-liquid composites in terms of grain boundary contiguity: 3. Causes and consequences of viscous anisotropy. *Journal of Geophysical Research: Solid Earth*, **114**, B06207.

Tasaka, M., Michibayashi, K. and Mainprice, D. (2008) B-type olivine fabrics developed in the fore-arc side of the mantle wedge along a subducting slab. *Earth and Planetary Science Letters*, **272**, 747–757.

Tasaka, M., Zimmerman, M.E. and Kohlstedt, D.L. (2016) Evolution of the rheological and microstructural properties of olivine aggregates during dislocation creep under hydrous conditions. *Journal of Geophysical Research: Solid Earth*, 121, 92–113.

Tielke, J.A., Zimmerman, M.E. and Kohlstedt, D.L. (2017) Hydrolytic weakening in olivine single crystals. *Journal of Geophysical Research: Solid Earth*, **122**, 3465–3479.

Tollan, P.M.E., O'Neill, H.S.C. and Hermann, J. (2018) The role of trace elements in controlling H incorporation in San Carlos olivine. *Contributions to Mineralogy and Petrology*, **173**, 89.

Tommasi, A. and Vauchez, A. (2015) Heterogeneity and anisotropy in the lithospheric mantle. *Tectonophysics*, **661**, 11–37.

Tommasi, A., Tikoff, B. and Vauchez, A. (1999) Upper mantle tectonics: three-dimensional deformation, olivine crystallographic fabrics and seismic properties. *Earth and Planetary Science Letters*, **168**, 173–186.

Tommasi, A., Mainprice, D., Canova, G. and Chastel, Y. (2000) Viscoplastic self-consistent and equilibrium-based modeling of olivine lattice preferred orientations: Implications for the upper mantle seismic anisotropy. *Journal of Geophysical Research – Solid Earth*, **105**, 7893–7908.

Tommasi, A., Langone, A., Padrón-Navarta, J.A., Zanetti, A. and Vauchez, A. (2017) Hydrous melts weaken the mantle, crystallization of pargasite and phlogopite does not: Insights from a petrostructural study of the Finero peridotites, southern Alps. *Earth and Planetary Science Letters*, **477**, 59–72.

Urai, J.L., Means, W.D. and Lister, G.S. (1986) Dynamic recrystallization of minerals. Pp. 161–199 in: *Mineral and Rock Deformation: Laboratory Studies (the Paterson volume)* (B.E. Hobbs and H.C. Heard, editors). American Geophysical Union, Washington, D.C.

Vannucci, R., Piccardo, G. B., Rivalenti, G., Zanetti, A., Rampone, E., Ottolini, L., Oberti, R., Mazzucchelli, M. and Bottazzi, P. (1995) Origin of LREE-depleted amphiboles in the subcontinental mantle. *Geochimica et Cosmochimica Acta*, **59(9)**, 1763–1771.

Vieira Duarte, J.F., Kaczmarek, M.-A., Vonlanthen, P., Putlitz, B. and Müntener, O. (2020) Hydration of a Mantle Shear Zone Beyond Serpentine Stability: A Possible Link to Microseismicity Along Ultraslow Spreading Ridges? *Journal of Geophysical Research: Solid Earth*, **125**, e2020JB019509.

Vissers, R.L.M., Drury, M.R., Strating, E.H.H., Spiers, C.J. and Vanderwal, D. (1995) Mantle shear zones and their effect on lithosphere strength during continental breakup. *Tectonophysics*, **249**, 155–171.

Wallis, D., Hansen, L.N., Tasaka, M., Kumamoto, K.M., Parsons, A.J., Lloyd, G.E., Kohlstedt, D.L. and Wilkinson, A.J. (2019) The impact of water on slip system activity in olivine and the formation of bimodal crystallographic preferred orientations. *Earth and Planetary Science Letters*, **508**, 51–61.

Wang, C., Liang, Y. and Xu, W. (2021) Formation of amphibole-bearing peridotite and amphibole-bearing pyroxenite through hydrous melt-peridotite reaction and in situ crystallization: an experimental study. *Journal of Geophysical Research: Solid Earth*, **126**, e2020JB019382.

Wang, J., Takahashi, E., Xiong, X., Chen, L., Li, L., Suzuki, T. and Walter, M.J. (2020) The water-saturated solidus and second critical endpoint of peridotite: implications for magma genesis within the mantle wedge. *Journal of Geophysical Research: Solid Earth*, **125**, e2020JB019452.

Warren, J.M. and Hirth, G. (2006) Grain size sensitive deformation mechanisms in naturally deformed peridotites. *Earth and Planetary Science Letters*, **248**, 438–450.

Wassmann, S. and Stöckhert, B. (2013) Rheology of the plate interface — Dissolution precipitation creep in high pressure metamorphic rocks. *Tectonophysics*, **608**, 1–29.

Wassmann, S., Stöckhert, B. and Trepmann, C.A. (2011) Dissolution precipitation creep versus crystalline plasticity in high-pressure metamorphic serpentinites. *Geological Society, London, Special Publications*, **360**, 129–149.

Watson, E.B. and Brenan, J.M. (1987) Fluids in the lithosphere. 1: Experimentally-determined wetting characteristics of CO_2-H_2O fluids and their implications for fluid transport, host-rock physical properties, and fluid inclusion formation. *Earth and Planetary Science Letters*, **85**, 497–515.

Whitney, D.L. and Evans, B.W. (2010) Abbreviations for names of rock-forming minerals. *American Mineralogist*, **95**, 185–187.

Wintsch, R.P. and Yi, K. (2002) Dissolution and replacement creep: a significant deformation mechanism in mid-crustal rocks. *Journal of Structural Geology*, **24**, 1179–1193.

Wyllie, P.J. and Ryabchikov, I.D. (2000) Volatile components, magmas, and critical fluids in upwelling mantle. *Journal of Petrology*, **41**, 1195–1206.

Zanetti, A., Vannucci, R., Bottazzi, P., Oberti, R. and Ottolini, L. (1996) Infiltration metasomatism at Lherz as monitored by systematic ion-microprobe investigations close to a hornblendite vein. *Chemical Geology*, **134**, 113–133.

Zhang, M., Niu, Y. and Hu, P. (2009) Volatiles in the mantle lithosphere: Modes of occurrence and chemical compositions. Pp. 171–212 in: *The Lithosphere: Geochemistry, Geology and Geophysics* (J.E. Anderson, editor). Nova Science Publishers Inc.

Zhang, S., Karato, S.-I., Fitz Gerald, J., Faul, U.H. and Zhou, Y. (2000) Simple shear deformation of olivine aggregates. *Tectonophysics*, **316**, 133–152.

Zimmerman, M.E. and Kohlstedt, D.L. (2004) Rheological properties of partially molten lherzolite. *Journal of Petrology*, **45**, 275–298.

Zimmerman, M.E., Zhang, S.Q., Kohlstedt, D.L. and Karato, S.-I. (1999) Melt distribution in mantle rocks deformed in shear. *Geophysical Research Letters*, **26**, 1505–1508.